Pre-loading of translation molecules onto ribosomes speeds transport and protein synthesis in *Escherichia coli*

Jennifer L. Hofmann,[1] **Theodore S. Yang**,[1] **Alp M. Sunol**[1] **Roseanna N. Zia**[1,2,*]
[1]Department of Chemical Engineering, Stanford University, Stanford, CA 94305
[2]Department of Mechanical and Aerospace Engineering, University of Missouri, Columbia, MO 65211
[*]Correspondence: rzia@missouri.edu

ABSTRACT

The rate of translation elongation in *Escherichia coli* is limited by diffusive transport of matching aminoacyl-tRNAs (aa-tRNAs) to ribosomes. Our previous work revealed that, as cell growth quickens, stoichiometric crowding speeds this diffusive search by optimizing encounters between cognate translation molecules, inclusive of chemical kinetics taken from *in vitro* experiments. However, we predicted absolute elongation rates three-fold slower than *in vivo* measurements. We hypothesized that 'pre-loading' of EF-Tu·GTP·aa-tRNA ternary complexes onto ribosomal L7/L12 subunits – suggested experimentally but not included in our initial model – might further speed elongation and close this gap. Here, we develop a first-principles physico-chemical model of the *E. coli* cytoplasm including explicit EF-Tu·L7/L12 interactions and elongation reaction kinetics, which quantitatively predicts *in vivo* binding and rheology. Our model reveals that transient co-localization of the translation machinery by EF-Tu·L7/L12 interactions shortens wait times at the ribosomal A-site, doubling elongation speed and improving prediction of the absolute elongation rate. We posit pre-loading efficiency as a competition between durable binding and frequent sampling of new ternary complexes, and show that the naturally-observed *E. coli* copy number of four L7/L12 subunits optimizes this tradeoff. Paired with literature data supporting a correlation between lower L7/L12 copy number and faster bacterial growth rate, we suggest a colloidal-scale evolutionary and functional advantage of having fewer L7/L12 per ribosome: frequent ternary complex sampling in dense, fast-growing cytoplasm.

INTRODUCTION

All cells must synthesize proteins to grow and divide. In fact, the translation process that produces proteins has been identified as the rate-limiting step of bacterial growth [1, 2]. As a result, faster-growing cells must produce proteins more rapidly, but the specific mechanism underlying this speedup was previously unknown.

A recent computational study of translation elongation [3] showed that the speedup with growth rate originates from colloidal-scale transport physics, and cannot be explained by chemical kinetics alone. Maheshwari et al. built a spatially-resolved physico-chemical model of the growth-rate dependent *Escherichia coli* cytoplasm (Fig. 1*A*), where Brownian motion and diffusion arise directly from first-principles physics. Each model 'translation voxel' contained ribosomes, EF-Tu·GTP·aa-tRNA (ternary complexes), and other native cytoplasmic proteins, at physiological abundances and densities extracted from whole-cell experiments [4–9]. Prior work [10] pointed to diffusive transport as a limiting factor in elongation but raised a paradox: faster-growing cells are more crowded (volume fraction $\phi_{\text{tot}} = 0.21$ to 0.42 at growth rate 1.0 to 3.0 dbl/hr), yet crowding slows diffusion. Resolving this paradox, Maheshwari et al. found that changing stoichiometry overcomes slowed diffusion, and indeed cooperates with packing to optimize encounters between cognate translation molecules. The underlying physical mechanism – termed 'stoichiometric crowding' – facilitates shorter diffusive search times of ternary complexes to ribosomes, thus speeding up the rate-limiting transport step of translation elongation [3].

Although the previous model showed that physics are required to predict the qualitative speedup, it under-predicted absolute elongation rates by at least three-fold compared to *in vivo*. This quantitative gap suggests additional mechanistic features of the searching and binding process yet to be explored. As an example, the original framework modeled only the purely steric interactions between translation molecules, whereas it is known that molecular surface chemistry produces attractive interactions between ribosomes and ternary complexes. Using structural and sequence homology-based methods, Rodnina and coworkers inferred an interaction between the C-terminal domain of ribosomal L7/L12 subunits and helix D of EF-Tu (Fig. 1*B*) that was found to slow elon-

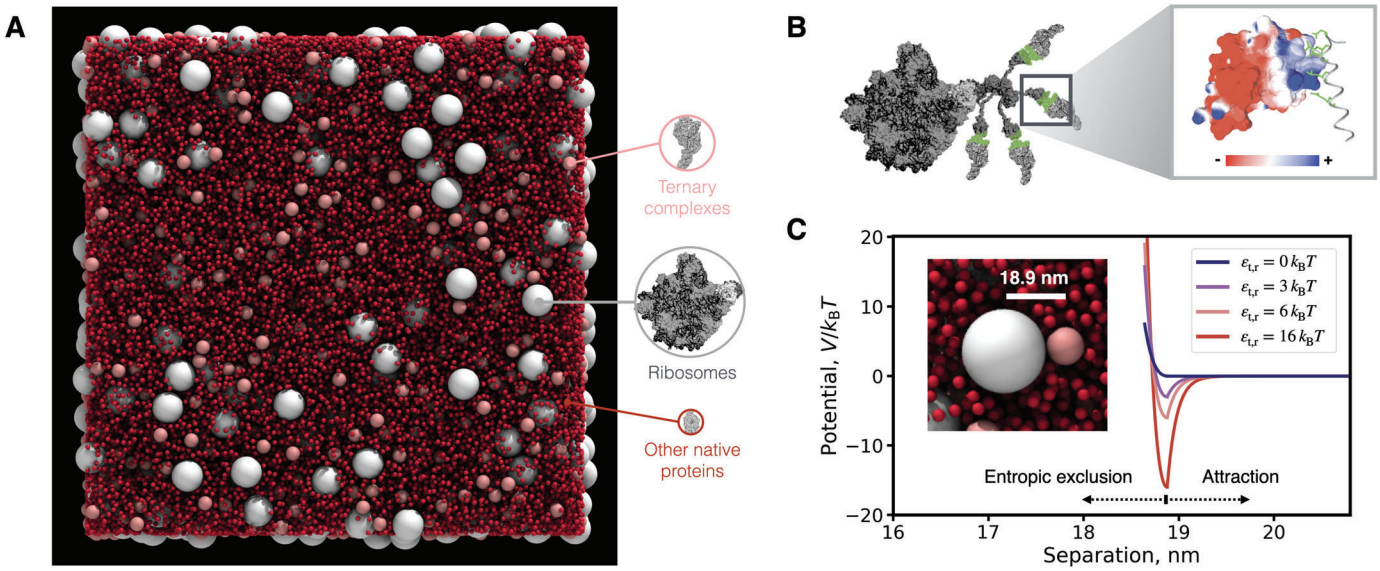

Figure 1: Dynamic simulation of colloidal "translation voxels" of the *Escherichia coli* cytoplasm, including biofidelic attractions between ternary complexes and ribosomes. *(A)* Visualization of a purely-repulsive isotropic hard sphere *E. coli* translation voxel at a growth rate of 1 dbl/hr, containing ribosomes (white), EF-Tu·GTP·aa-tRNA ternary complexes (pink), and other native cytoplasmic proteins (red). Protein abundances and volume measurements were compiled from experiments by [3]. Molecular representations adapted with permission from [14], and [19, 20] under a CC-BY-4.0 license. *(B)* Structural models of ternary complex binding to L7/L12 ribosomal subunits in *E. coli*. (Inset) Contact scheme between the C-terminal domain of a L7/L12 subunit (surface representation on left) and EF-Tu helix D in the ternary complex (ribbon structure on right), adapted with permission from [13]. The surface representation is colored according to charge (red, negative; blue, positive). *(C)* The binding interaction is modeled via an isotropic pair-wise potential consisting of the repulsive part of a Morse potential to ensure entropic exclusion at contact (the sum of particle radii, σ_{ij}), and an attractive Yukawa potential (Eq. 1). A number of potential well depths are studied in this work, from $\varepsilon_{\mathrm{t,r}} = 0 - 16\,k_{\mathrm{B}}T$ (colors, inset legend).

gation upon mutation [11–14]. In this work, we focus on these EF-Tu·L7/L12 interactions, which are implicated in binding multiple ternary complexes to each ribosome prior to entry into the A-site [15–17].

To translate efficiently, a ribosomal A-site should not have to wait longer than necessary to test a new aa-tRNA. This wait time is set by the diffusive search time that brings a ternary complex close enough to the ribosome for cognate testing to occur. Stoichiometric crowding shortens this wait time as cell growth quickens by bringing more advantageous stoichiometry into closer proximity [3]. We hypothesize that EF-Tu·L7/L12 interactions promote and preserve this advantageous co-localization, thereby further reducing ribosomal wait times and supporting faster absolute elongation rates.

To rapidly load an unoccupied A-site, co-localized ternary complexes must remain near a ribosome over time scales comparable to the initial aa-tRNA recognition test (lasting micro- to milliseconds, [3]). Thus, elucidating a mechanism by which ternary complexes are 'pre-loaded' onto ribosomes requires interrogation at the mesoscale – connecting microscopic interaction details over nanometers, to dynamics over milliseconds. Experimental methods are limited at this scale: structural techniques provide molecular-level interaction details but are only static snapshots [15]. Particle-tracking methods reveal dynamics but cannot capture motions faster than 2 ms or spatial detail below 60 nm, precisely the length- and timescales over which co-localization of translation molecules occurs [17]. Colloidal simulations can readily model this mesoscale regime [18], thereby mechanistically connecting 'pre-loading' of ternary complexes onto ribosomes to bulk cellular behaviors.

Here we expand the simulation framework developed by Maheshwari et al. [3] to efficiently incorporate attractions between ternary complexes and ribosomes in translation voxels of the *E. coli* cytoplasm. Informed by established biochemical data, we estimated the physiological EF-Tu·L7/L12 attraction strength to be $\sim 16\,k_{\mathrm{B}}T$ (Fig. 1*C*, see ***Methods***). We implemented this attraction via two fundamental models. In the first, the attractive potential is distributed isotropically over molecular surfaces. In the second, we limited the valency to exert attractions only between discrete surface patches, tailored to represent the L7/L12 and EF-Tu binding sites. Our results demonstrate that this interaction valency must be limited to recover *in vivo* localization, kinetic, and dynamic measurements, and to avoid cytoplasmic arrest. We show that EF-Tu·L7/L12 interactions transiently co-localize the translation machinery, thereby reducing wait times at the ribosomal A-site and speeding protein synthesis. We close with a discussion of the broader implications of our work, supporting a colloidal-scale physical basis for cellular fitness.

RESULTS

Strong isotropic attractions between translation molecules fully arrest the cytoplasm

We began with the simplest model: isotropic binding interactions between ternary complexes and ribosomes, with an attraction strength corresponding to the experimentally-predicted value ($\varepsilon_{\mathrm{t,r}} = 16\,k_{\mathrm{B}}T$, see ***Methods***). We implemented this interaction potential (Fig. 1*C*) in our translation voxel model of the *E. coli* cytoplasm, which also includes a physiological distribution of non-attracting proteins. Visual inspection of the cytoplasm reveals that these strong isotropic attractions cause gelation: ternary complexes and ribosomes self-assemble into a space-spanning network across all studied cellular growth rates (Fig. 2*A*). To confirm the structural features of gelation, we calculated the static structure factor $S(q)$, which describes the distribution of density correlations at a given wavevector q or real space length $l = 2\pi/q$ (Eq. 6). Gels exhibit a dominant abundance of long-range structure compared to a suspension of freely mobile molecules. We observed peaks at length scales $100\,\mathrm{nm} \lesssim l \lesssim 200\,\mathrm{nm}$, indicating formation of large aggregates and networks (vertical dotted lines, Fig. 2*A*). The peak shifts to smaller length scales at faster cellular growth rates and higher cytoplasmic volume fractions, corresponding with thinner gel strands and smaller interstitial pores. These results are consistent with prior studies of nonliving colloidal gels, where strong isotropic attractions cause deep arrest of phase separation [22] and formation of fine, vitrified structure [23].

We next verified that gelation occurred by testing cytoplasm rheology. We calculated the effective viscosity experienced by ternary complexes as a function of cellular growth rate, accounting for the quantitative influences of hydrodynamic and confinement effects (Eq. 9). Without attractions ($\varepsilon_{\mathrm{t,r}} = 0\,k_{\mathrm{B}}T$), the effective viscosity exhibits the expected increase with volume fraction and cellular growth rate (left to right, Fig. 2*C*) as the cytoplasm densifies [3]. However, without attractions, the model underpredicts by two- to three-fold the *in vivo* estimate for equivalently-sized proteins in *E. coli* [21] (horizontal dotted line, Fig. 2*C*). In contrast, we found that strong isotropic attractions ($\varepsilon_{\mathrm{t,r}} = 16\,k_{\mathrm{B}}T$) lead to over-prediction of viscosity, up to two orders of magnitude more than *in vivo* estimates. The mechanistic origin of this behavior is the connection between viscosity and particle mobility – more precisely, the molecular diffusivity.

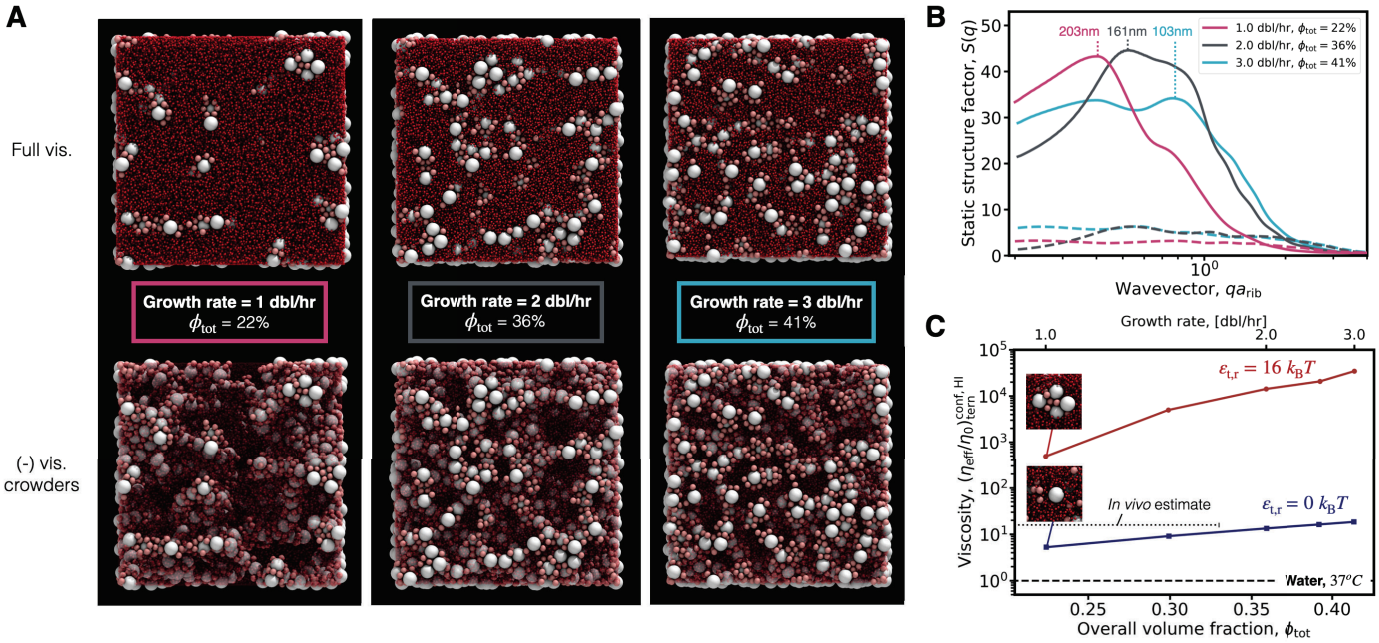

Figure 2: Strong isotropic attractions between ternary complexes and ribosomes drive cytoplasmic arrest across all studied growth rates. *(A)* Visualizations of *E. coli* translation voxels with strong isotropic attractions ($\varepsilon_{\mathrm{t,r}} = 16\,k_{\mathrm{B}}T$) between ternary complexes and ribosomes at three growth rates (left to right). ϕ_{tot} is the total system volume fraction, which increases from 22% to 41% as cell growth rate increases. (Upper) Full visualization with ribosomes (white), ternary complexes (pink), and other native cytoplasmic proteins (red). (Lower) Visualizations with transparent native cytoplasmic proteins, highlighting the internal voxel microstructure. *(B)* Static structure factor, $S(q)$, (Eq. 6) for growth rates of 1 (magenta), 2 (grey), and 3 dbl/hr (blue) for the hard sphere ($\varepsilon_{\mathrm{t,r}} = 0\,k_{\mathrm{B}}T$, dashed lines) and strongly attractive ($\varepsilon_{\mathrm{t,r}} = 16\,k_{\mathrm{B}}T$, solid lines) cases. The peak, corresponding to the most abundant suspension length scale in real space, is marked with vertical dotted lines. *(C)* Effective cytoplasmic viscosity, η_{eff}, experienced by ternary complexes in translation voxels (Eq. 9), versus growth rate and volume fraction for the hard sphere (blue) and strongly attractive (red) cases. The viscosity of water, η_0, at a temperature of $37^{o}C$ (horizontal dashed line) and the estimated *in vivo* viscosity experienced by a protein with a molecular weight of 69 kDa (M_{tern}) in *E. coli* (horizontal dotted line, [21]) are marked.

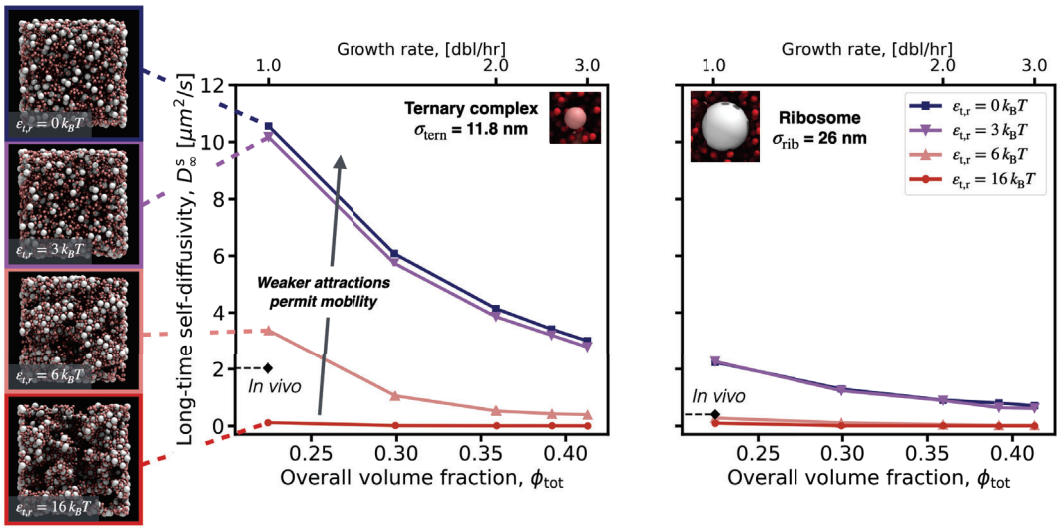

Figure 3: Isotropic attractions weak enough to avoid arrest permit faster diffusion than measured *in vivo*. The long-time self-diffusivity (Eq. 7) for ternary complexes (left) and ribosomes (right) as a function of growth rate and total volume fraction ϕ_{tot} , with isotropic attractions of strength $\varepsilon_{\text{t,r}} = 0 - 16\,k_{\text{B}}T$ (colors, inset legend). The experimentally-observed apparent diffusivity is shown for a growth rate of 1.0 dbl/hr (♦) for both ternary complexes and ribosomes [17]. Simulation screenshots of translation voxels at 1.0 dbl/hr at each studied attraction strength are shown (inset, left).

We quantified molecular dynamics by measuring mean-square displacement over time (*SI Appendix*, Fig. S4) and, from it, computing the long-time self-diffusivity of translation molecules (Eq. 7). We performed this calculation in translation voxels over a range of cellular growth rates, accounting for hydrodynamics and confinement. With strong isotropic attractions ($\varepsilon_{\text{t,r}} = 16\,k_{\text{B}}T$), we found that ternary complexes diffuse seventeen-fold slower than *in vivo* measurements, and ribosomes diffuse four-fold slower [17] (Fig. 3). These results are consistent with the high effective viscosities reported above. Overall, our results show that strong isotropic attractions between translation molecules arrest cytoplasm dynamics, rendering them too slow to support protein synthesis.

We next searched for an isotropic attraction strength that would avoid gelation and produce dynamics comparable to *in vivo* measurements. We again computed the long-time self-diffusivity of ternary complexes and ribosomes (Fig. 3) in translation voxels at a range of growth rates, and for three weaker attraction strengths ($\varepsilon_{\text{t,r}} = 0, 3$, and $6\,k_BT$). *In vivo* data are available for only one growth rate, 1dbl/hour [17], shown as a single data point. As expected, diffusivity decreases with increased crowding. Our results suggest that an isotropic attraction strength must be greater than $\varepsilon_{\text{t,r}} = 6\,k_{\text{B}}T$ to match the *in vivo* diffusivity, but would still produce gelation (Fig. 3, screenshots to left; *SI Appendix*, Fig. S2, Movie S1). Evidently, the strength of isotropic attractions cannot be tuned to recover the slow *in vivo* dynamics of translation molecules without cytoplasmic arrest. We inferred here that some other attraction mechanism is required to enable durable, yet short-ranged co-localization of ternary complexes and ribosomes.

Attractions must induce short-range, durable co-localization

We quantified the co-localization of translation molecules by calculating the fraction of ternary complexes bound to ribosomes in our simulations (Eq. 10). We compared our results to the limited available *in vivo* data at 1 dbl/hr, which indicates approximately 60% of ternary complexes are bound at any given instant [17]. We first examined how physical size contributes to co-localization, without attractions between ternary complexes and ribosomes ($\varepsilon_{\text{t,r}} = 0\,k_{\text{B}}T$, Fig. 4*A*). Co-localization increases with crowding at faster growth rates, driving up the fraction of bound ternary complexes from 4% (at 1 dbl/hr) to 16% (at 3 dbl/hr). This growth-rate dependence and its underpinning in stoichiometric crowding is consistent with the recently-established mechanistic origin of the speedup of translation in *E. coli* [3].

A crucial aspect of both that study and our present one is that the key behavior cannot be recovered without explicit representation of smaller cytoplasmic proteins. Here, through study of the pair distribution function (*SI Appendix*, Fig. S5), we found that entropic forces alone can drive co-localization by inducing a $1\,k_{\text{B}}T$ depletion interaction between ternary complexes and ribosomes. The strength of this depletion effect remains fixed across growth rates even as molecular stoichiometry and overall crowding change. However, the absolute volume fraction of smaller cytoplasmic proteins remains relatively constant across growth rates [3], which

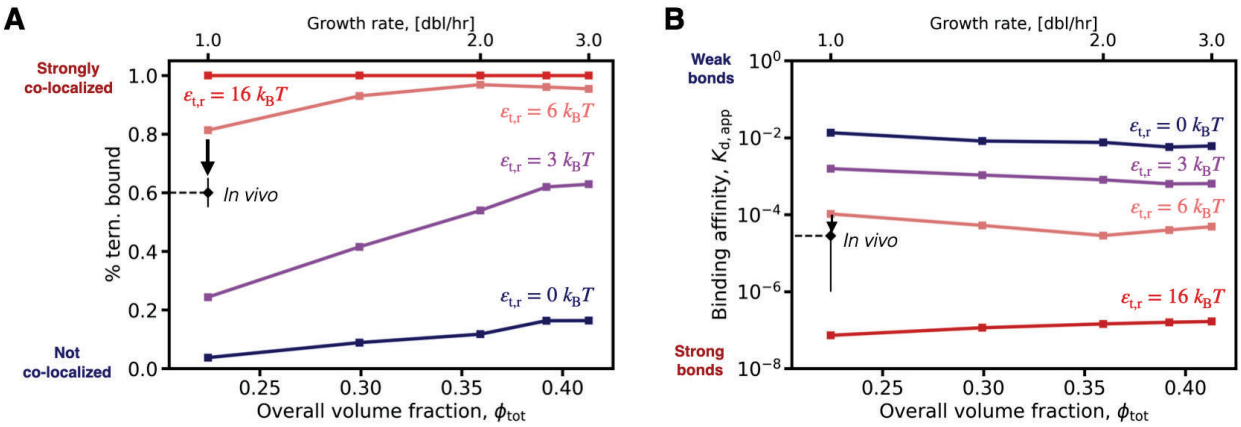

Figure 4: Physical co-localization and biochemical affinity measurements. *(A)* Percent of ternary complexes bound to ribosomes (Eq. 10) for isotropic attraction strengths of $\varepsilon_{t,r} = 0 - 16 k_BT$ (colors). Stronger attractions drive more co-localization of translation molecules, and suggest that an isotropic attraction strength less than $\varepsilon_{t,r} = 16\ k_BT$ would best recover experimental measurements at a growth rate of 1.0 dbl/hr (♦) [17]. *(B)* Apparent equilibrium dissociation constant $K_{d,app}$ (Eq. 11) for the interaction between ternary complexes and ribosomes, with isotropic attraction strengths of $\varepsilon_{t,r} = 0 - 16\ k_BT$ (colors). Stronger attractions drive stronger binding affinities, and suggest that an isotropic attraction strength greater than $\varepsilon_{t,r} = 6\ k_BT$ would best recover experimental measurements at a growth rate of 1.0 dbl/hr (♦) [17].

sets the 'free volume' that induces entropic depletion attractions. Ultimately, attractions on the order of a few k_BT are not strong enough to suppress the bond-breaking action of Brownian motion. The total fraction of bound ternary complexes in this non-attractive limit, as well as the weak isotropically attractive case ($\varepsilon_{t,r} = 3\ k_BT$), is well below the *in vivo* estimate (Fig. 4*A*).

In contrast, when isotropic attractions are strong compared to Brownian motion ($\varepsilon_{t,r} = 16\ k_BT$), bonds are essentially permanent and 100% of ternary complexes are bound to ribosomes at a given instant (Fig. 4*A*). But between the non-attractive and strongly attractive limits, bonds that are broken by Brownian motion easily re-form. We found that when attractions are six-fold stronger than thermal fluctuations ($\varepsilon_{t,r} = 6\ k_BT$), binding wins on average: 80% of ternary complexes are bound to ribosomes in simulations at 1 dbl/hr (Fig. 4*A*). However, the bound percentage still exceeds the *in vivo* estimate (60±5% bound, [17]). This macroscopic view of co-localization suggests that an isotropic attraction strength between 3 and $6\ k_BT$ would best represent the interaction inside cells.

To refine this estimate, we examined bond durability more directly. We calculated the apparent binding affinity, $K_{d,app}$, of the interaction between ternary complexes and ribosomes in our simulations (Eq. 11) and compared to the *in vivo* estimate at 1 dbl/hr [17]. This bond-focused approach results in an apparent paradox. Attraction strength must be greater than $6\ k_BT$ to recover the experimental binding affinity, in contrast to the prediction from macroscopic co-localization measurements (Fig. 4*B*).

To resolve this paradox, we shifted from the bulk perspective to a microscopic, ribosome-centric view. We calculated the coordination number, N_c, of each ribosome – i.e., the number of ternary complexes to which it is bound (*SI Appendix*, Fig. S6). In *E. coli*, ribosomes interact with EF-Tu in ternary complexes via four L7/L12 subunits (Fig. 1*B*, [13, 17]), and are negatively charged elsewhere [24, 25]. We thus expect a maximum coordination number of four, assuming one ternary complex binds to each L7/L12. However, we found that strong isotropic attractions ($\varepsilon_{t,r} = 16\ k_BT$) produce a broad distribution of coordination numbers, including a high probability of $7 \leq N_c \leq 15$ (*SI Appendix*, Fig. S6). This clearly unphysical result was not resolved by reducing the attraction strength to $6\ k_BT$. Even weaker isotropic attractions ($\varepsilon_{t,r} = 0 - 3\ k_BT$) produce insufficient coordination numbers with peaks at $0 \leq N_c \leq 2$. Our results affirm that an isotropic attraction distribution is a poor model for interactions between translation molecules, in which ternary complexes are permitted to bind over the entire ribosome surface.

We hypothesized that a limited attraction valency could resolve the paradox in co-localization and affinity measurements. Strong attractions, when limited to small patches on molecular surfaces, could drive co-localization with a narrower distribution of coordination numbers. Gelation could thereby be prevented, while maintaining high affinity individual bonds.

Limited-valency attractions prevent arrest and recover physiological dynamics and microstructure

To test our hypothesis, we developed a limited valency model for interactions between ternary complexes and ribosomes. "Limited valency" here means that attractions are confined to discrete surface patches, rather than being distributed isotropically over

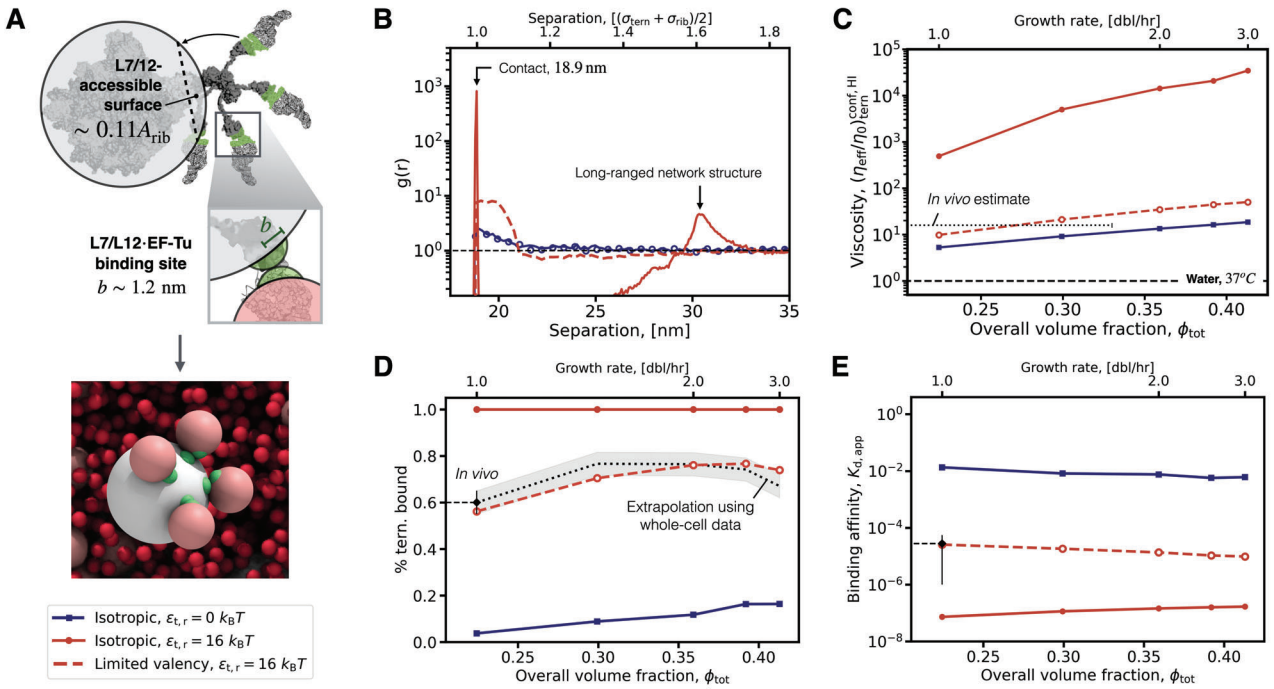

Figure 5: Limited-valency attractions recover physiological levels of co-localization and binding affinity, while avoiding cytoplasmic arrest. *(A)* Visualization of the limited-valency model, where attractions between ternary complexes (pink) and ribosomes (white) are restricted to binding sites (green), sized to match that of structural measurements (upper). Please see ***Methods*** for detailed calculations of the L7/L12 accessible surface area ($\sim 11\%$ of the total surface area $A_{\rm rib}$) and the size of the binding sites (of radius $b \sim 1.2\,{\rm nm}$). *(B)* Radial distribution functions, $g(r)$, (Eq. 5) between ternary complexes and ribosomes at a growth rate of 1 dbl/hr and $\phi_{\rm tot}$ = 22%. The non-attractive limited-valency case (blue, symbols) quantitatively recovers the microstructure of the non-attractive isotropic case (blue, solid line). Strong isotropic attractions (red, solid line) produce a high probability of finding a ternary complex and ribosome at contact, as well as a second peak corresponding to formation of long-ranged network structure. Strong limited-valency attractions (red, dashed line) increase the contact peak versus the non-attractive case, while avoiding the second peak. *(C)* Effective cytoplasmic viscosity (Eq. 9) experienced by ternary complexes, versus growth rate and volume fraction. The viscosity of water, η_0, at a temperature of 37^oC (horizontal dashed line) and the estimated *in vivo* viscosity of a protein equal in size to a ternary complex in *E. coli* (horizontal dotted line [21]) are marked. *(D)* The percent of ternary complexes bound to ribosomes (Eq. 10), as a function of growth rate. The experimentally-measured value is marked for a growth rate of 1.0 dbl/hr (♦) [17], and extrapolated to higher growth rates (dotted black line) as described in *SI Appendix* and Fig. S10. *(E)* The apparent equilibrium dissociation constant $K_{\rm d,app}$ for the interaction between ternary complexes and ribosomes (Eq. 11), as a function of growth rate.

a molecule. In our model, we restricted binding sites on the ribosome to four distinct spherical caps of radius $1.2\,{\rm nm}$, and to a single binding site on the ternary complexes of the same size. We computed this binding site size as the width of the L7/L12 C-terminal domain (Fig. 5*A*), as described in ***Methods***. Interaction between any other part of a ternary complex and ribosome is strictly entropic, i.e., hard-sphere repulsion prevents overlap. We comment that these translation molecules are negatively charged, creating a longer-ranged repulsion than simple hard-sphere exclusion; it is straightforward to generalize our model to explore these effects but is beyond the scope of this study.

We deployed the limited valency framework into dynamic simulations translation voxels of the *E. coli* cytoplasm. We first investigated whether limited binding valency prevents cytoplasmic arrest. Hallmark correlations in positions among particles – microstructure [26, 27] – are associated with purely-repulsive, liquid-like, and gelled suspensions. One way to quantify this structure is the radial distribution function, $g(r)$, (Eq. 5) which here describes the probability of finding a ternary complex and ribosome pair at a given separation. We first calculated $g(r)$ for the baseline model of an isotropic non-attracting suspension, focusing on the slowest growth rate with cytoplasmic volume fraction $\phi_{\rm tot} = 22\%$ (Fig. 5*B*). Next, we tested our limited valency framework by adding the binding sites but suppressing attractions. The non-attractive limited-valency data overlay the baseline curve, validating that the patchy protrusions themselves do not change cytoplasmic microstructure.

Next, we turned on the $16\,k_{\rm B}T$ attractions between binding sites, which tripled the probability of finding ternary complexes in contact with ribosomes (Fig. 5*B*). The width of the nearest-neighbor peak corresponds to the range of solid angles of the bond between protruding binding sites. We next compared against our original isotropic model with $16\,k_{\rm B}T$ attractions. We observed a sharp peak

at contact and an abundance of long-range structure, both hallmarks of a gel network. Importantly, this long-ranged peak is absent for the limited valency model, indicating that patchiness prevents gelation under these conditions. We confirmed the absence of large cytoplasmic aggregates via calculation of the static structure factor, $S(q)$ (*SI Appendix*, Fig. S8*A*). Our results thus demonstrate that strong limited-valency attractions drive short-ranged co-localization of ternary complexes and ribosomes, while avoiding gelation.

The degree of long-range structure affects cytoplasmic rheology. Here, we examined the impact of interaction valency on the viscosity as a function of cellular growth rate, via the same approach used for Fig. 2*C* (Eq. 9). Strong $16\,k_{\mathrm{B}}T$ patchy attractions drive up the effective viscosity two- to three-fold compared to the case with no attractions (Fig. 5*C*). Moreover, the limited valency model with experimentally-inferred attraction strength and patch structure accurately recovers the *in vivo* estimate (horizontal dotted line, Fig. 5*C*). Limiting the interaction valency thus prevented unphysiological cytoplasmic viscosities and recovered macroscopic experimental behavior.

We next examined the microscopic impacts of limited-valency attractions on short-range co-localization. As initially reported in Fig. 4*A*, we found that no attractions and strong isotropic attractions produced too few and too many bound ternary complexes, respectively, as compared to the *in vivo* data. However, with $16\,k_{\mathrm{B}}T$ limited-valency attractions, we found that 56% of ternary complexes are bound to ribosomes at a growth rate of 1 dbl/hr (Fig. 5*D*, Eq. 10), in good agreement with the *in vivo* measurement of $60 \pm 5\%$ [17]. Since *in vivo* data are available only for a single growth rate, we extrapolated the measurement to higher growth rates by accounting for changes in molecular stoichiometry and crowding (*SI Appendix*, Fig. S10). Our limited-valency model agrees very well with this *in vivo* extrapolation.

The model captures the non-monotonic trend of the *in vivo* data (Fig. 5*D*). As cell growth speeds up from slow to moderate growth rates, more ternary complexes are bound to ribosomes – an entropic effect dominated by densification of the cytoplasm (Fig. 4*A*, $\varepsilon_{\mathrm{t,r}} = 16\,k_{\mathrm{B}}T$). Approaching the fastest growth rates, the increase in the abundance of ternary complexes outpaces that of ribosomes [3]. Thus, even if ribosomal binding sites are saturated, there are more 'free' ternary complexes at the fastest growth rates. Even though crowding increases, the changed stoichiometry reduces the relative fraction of ternary complexes bound to ribosomes. The underlying microscopic picture is revealed in Fig. S11 (*SI Appendix*), where patchiness drives the mean coordination number of the ribosome toward the physiological limit of $N_{\mathrm{c}} = 4$. Recall that for isotropic $16\,k_{\mathrm{B}}T$ attractions, we observed unphysical coordination numbers of $0 \leq N_{\mathrm{c}} \leq 15$ with $\langle N_{\mathrm{c}} \rangle \approx 6$. With a limited attraction valency, we found coordination numbers $N_{\mathrm{c}} \lesssim 4$, confirming measured and expected results. Moreover, the limited-valency model quantitatively recovers the *in vivo* binding affinity of $K_{\mathrm{d,app}} \sim 28\,\mu\mathrm{M}$ [17] (Fig. 5*E*, Eq. 11).

Co-localization must be dynamic, otherwise irreversible binding of ternary complexes to ribosomal L7/L12 subunits would prevent rapid combinatoric testing of aa-tRNAs. Transient binding, however, could facilitate near-immediate loading of an unoccupied A-site, thus shortening the diffusive search process. Such rapid loading would require physical binding events that are comparable in duration to the initial aa-tRNA recognition test (lasting from 0.001 to $10\,\mathrm{ms}$ [3], see *SI Appendix*). In our limited-valency model, we quantified the duration of physical binding events between ternary complexes and ribosomes and observed two key features (*SI Appendix*, Fig. S12). First, a short-duration peak from 0.001 to $0.01\,\mathrm{ms}$ is driven purely by entropic forces. Second, limited-valency attractions induce a wide plateau of binding event durations from 0.01 to $1\,\mathrm{ms}$, which corresponds well to the timescale of the initial recognition test. These results support a previous inference from *in vivo* particle tracking experiments [17] that ternary complexes can bind to the L7/L12, be tested, and unbind within $2\,\mathrm{ms}$.

EF-Tu·L7/L12 interactions facilitate translation by speeding up colloidal-scale transport

We next simulated limited-valency attractions alongside intra-ribosomal chemistry to directly test how pre-loading on L7/L12 subunits impacts elongation latency. To do so, we expanded our physics-based model to incorporate the reaction framework developed by Maheshwari et al. [3]. In simulation, molecules experience physical interactions and undergo chemical reactions that represent the multi-step kinetics leading to peptide bond formation (see ***Methods***). To fully represent physiological cytoplasm, we accounted for differences in cognate, near-cognate and non-cognate ternary complexes, and represented the *in vivo* distribution of relative

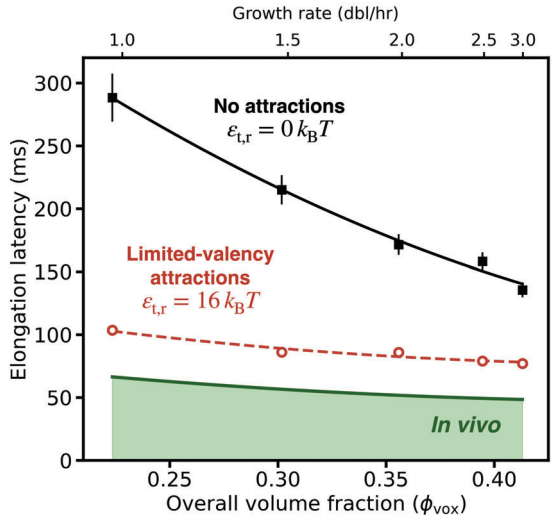

Figure 6: Pre-loading of ternary complexes onto ribosomes works alongside stoichiometric crowding to speed elongation. Initial simulations of hard-sphere translation voxels (black symbols, [3]) recovered the qualitative speedup in elongation latency measured *in vivo* (green line, [4]). Limited-valency attractions drive two- to three-fold shorter elongation latencies (red symbols, dashed line; this work), and improve agreement with experiments. Error bars corresponding to SEM are on the order of marker size in the limited-valency case.

codon and tRNA abundances over thousands of voxel simulations. By tracking the time a ternary complex spends in and outside of reactions before it encounters its matching ribosome, we obtained a measure of elongation latency (τ_{elong}) that is comparable to *in vivo* measurements [4].

We found that limited-valency attractions between ternary complexes and ribosomes speed up elongation latency by two- to three-fold compared to our original model [3] (Fig. 6). We note that this decrease emerges entirely from shortened transport latency (see *SI Appendix*, Fig. S14). EF-Tu·L7/L12 interactions thus shorten the time ribosomes must wait to find a matching ternary complex.

The predicted speedup with growth rate now shows quantitative agreement with *in vivo* measurements. These results provide further support to the finding that stoichiometric crowding speeds protein synthesis in faster-growing *E. coli*. The absolute rate of elongation, however, can be modulated by other physico-chemical mechanisms, including pre-loading of ternary complexes onto ribosomal L7/L12 subunits.

L7/L12 copy number optimizes ternary complex binding and sampling

Finally, we asked how having varied L7/L12 copy numbers c might impact translation elongation in *E. coli*. We built limited-valency ribosome models with two, six, and eight binding sites, corresponding to the case when one L7/L12 dimer is knocked out in *E. coli* ($c = 2$) [30] and physiological stoichiometries in other bacteria ($c = 6, 8$) [29]. In simulations of translation voxels at 3 dbl/hr, we found that binding events between ternary complexes and ribosomes last up to milliseconds when copy number $c \geq 4$, (green shaded region, Fig. 7*(A)*). These results indicate that higher copy numbers are sufficient to pre-load ternary complexes and reduce ribosomal wait times, as observed earlier for the $c = 4$ case. The knock-out case, $c = 2$, dramatically reduces encounter durations, which we hypothesize are well below the times required for effective pre-loading.

However, durable co-localization can come at the cost of rapid combinatoric sampling of new ternary complexes (Fig. 7*(B)*). We calculated the fraction of the entire ternary complex population that each ribosome samples, i.e., binds with, in limited-valency voxels with $c = 2 - 8$. Whereas the knock-out case maintains high sampling of 87% of ternary complexes, the higher copy number cases ($c = 6, 8$) are limited to sampling only 55% and 45% of the combinatoric space, respectively (Fig. 7*(B)*). In the physiological $c = 4$ case, we found that ribosomes are still able to sample 85% of ternary complexes on average, despite supporting a population of long-duration binding events.

To summarize this tradeoff between binding and sampling, we calculated the product of the bound and freely mobile ternary complex states represented in Fig. 7*(A)-(B)*, and plotted this product in Fig. 7*(C)*. Beyond the physiological copy number of four L7/L12 per ribosome, we found that the benefits of co-localization (shorter ribosomal wait times) are outpaced by the deleterious effects of limiting ternary complex mobility (less sampling of new ribosomes) at the densest, fastest *E. coli* growth rate. That is, $c = 4$ is the

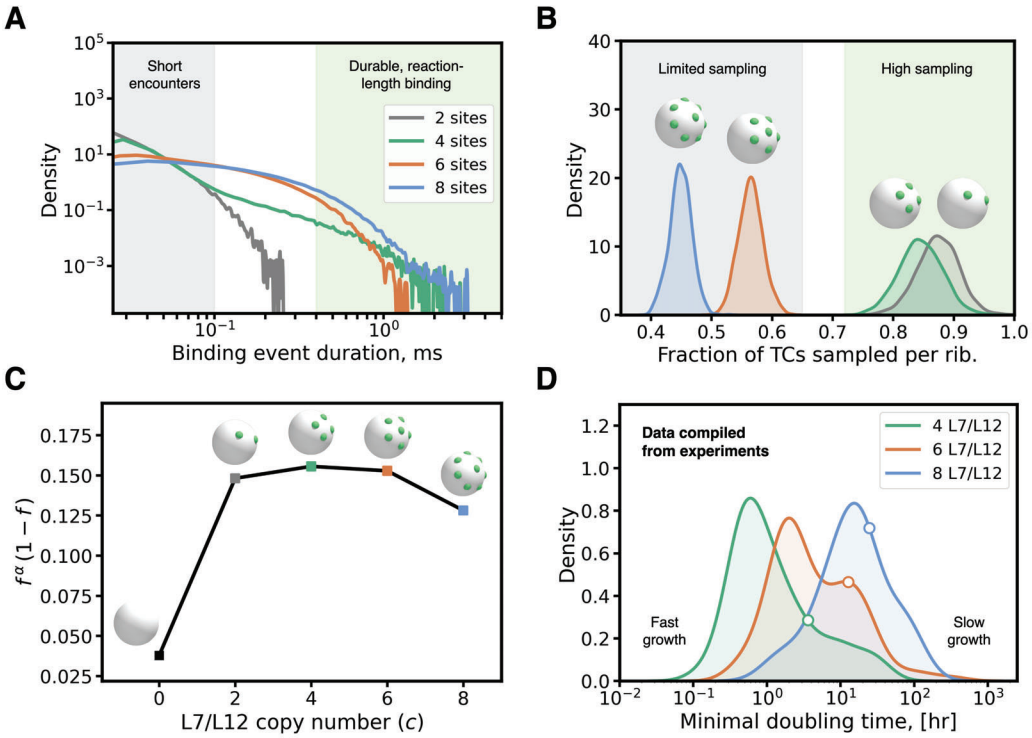

Figure 7: L7/L12 copy number optimizes binding and sampling in *E. coli*, and may support faster growth rates across bacteria. (A) Probability density function (shown as the kernel density estimate, KDE) of the duration of binding events, defined as when a ternary complex and ribosome come within a bond distance of $2.1\ \mathrm{nm}$ from contact. As the ribosome is functionalized with more binding sites representing a higher L7/L12 copy number c (colors), ternary complexes remain bound to ribosomes for longer durations (arrow, inset). The physiological copy number ($c = 4$ sites) produces binding events with durations comparable to the initial aa-tRNA recognition test (green background), the desired binding length. **(B)** KDE of the fraction of the entire ternary complex population that each ribosome samples, i.e., binds with, for each L7/L12 copy number (colors; model schematics, inset). The physiological copy number ($c = 4$ sites) permits ribosomes to maintain a high sampling rate of ternary complexes (green background). **(C)** The tradeoff between bound and freely searching ternary complexes in *E. coli* translation voxels at a growth rate of 3 dbl/hr, as a function of L7/L12 copy number c (model screenshots, inset), where f is the fraction of ribosome-bound TCs and $\alpha = 1.71$ is the ratio of Boltzmann state energies that produces $f^{in\ vivo}$ (see Methods). The physiological case ($c = 4$) maximizes this tradeoff. **(D)** KDE of minimal doubling time for $N = 354$ bacteria [28] with known L7/L12 copy number (colors, inset legend; [29]). Bacteria with fewer L7/L12 tend to have faster doubling times. The mean minimal doubling times for each L7/L12 copy number distribution (white circles) were compared using the Mann-Whitney U-test ($p < 0.001$ in all cases).

optimal copy number in our simulations, as well as in real *E. coli*. In the **Discussion**, we speculate about how a copy number of four L7/L12 might have evolved to maximize this tradeoff and support faster growth rates more broadly.

DISCUSSION

The speed-up in per-ribosome elongation rate as *E. coli* growth quickens originates from a physical mechanism by which advantageous molecular stoichiometry is brought into closer proximity [3]. This 'stoichiometric crowding' effect optimizes encounters between cognate translation molecules, shortening the diffusive search time of ternary complexes to ribosomes. However, an approximately three-fold gap between predicted and measured elongation latencies [4] suggested additional mechanisms might further speed elongation by facilitating this searching and binding process.

We hypothesized that interactions between ribosomal L7/L12 subunits and EF-Tu in ternary complexes [11–16] could augment this advantageous co-localization and further shorten the time a ribosome must wait to test a new aa-tRNA. To this end, we built a dynamic computational model that efficiently incorporated attractions between ternary complexes and ribosomes in voxels of the growth-rate dependent *E. coli* cytoplasm. Our model enabled interrogation of transient binding dynamics at higher resolution than currently accessible by particle tracking methods [17]. We applied our model to mechanistically connect microscopic interaction details to bulk cellular behaviors, i.e., elongation rate.

We first found that limited-valency attractions representing the physiological binding of EF-Tu to L7/L12 drive durable co-localization of the translation machinery, while avoiding cytoplasmic arrest. Next, we showed that L7/L12 subunits serve a central role in setting the rate of protein synthesis by 'pre-loading' ternary complexes onto the ribosome and halving the elongation rate. These results demonstrate a cooperation between ribosomal structure and stoichiometric crowding that speeds per-ribosome productivity.

Additional physico-chemical mechanisms could explain the remaining quantitative gap between predicted and measured elongation latency, including attractions between mRNA codons and tRNA anticodons [31] that could 'pre-sort' cognate ternary complexes near ribosomes. Modest discrepancies between the *in vitro* chemical kinetic parameters used in our model and real *in vivo* rates – arising, for example, from differences in solvent conditions – could also close the gap [3]. Future work might further refine physical interaction details to include representation of surface roughness, repulsions between negatively charged tRNA and rRNA, or the mobility of the L7/L12 arms. We note that experimental data for dynamics and co-localization are limited to a single growth rate in our studied range [17]. Additional *in vivo* data at faster *E. coli* growth rates would enable further validation of crowding-dependent behaviors in our model.

An evolutionary advantage is implicated by the physiological *E. coli* copy number of four ribosomal L7/L12 subunits, given the hypothesis that the last bacterial common ancestor had six L7/L12 [29]. Here, we demonstrated a putative mechanism underlying this phenotype, finding that four L7/L12 copies optimize durable binding and frequent sampling of new ternary complexes in dense *E. coli* cytoplasm. Higher copy numbers of six and eight L7/L12 favor binding over sampling. Given the comparatively fast doubling time of *E. coli*, we were curious if this high sampling frequency correlates with fast cellular growth more broadly. Across a set of 354 bacteria, we found that organisms with fewer L7/L12, such as *E. coli* and *Clostridium perfringens*, tend to be faster growing than those with more L7/L12, such as the cyanobacteria *Trichodesmium erythraeum* and *Gloeobacter violaceus* (Fig. 7*(D)*). If the densification of cytoplasm with growth rate is a general feature of bacteria, we speculate that a copy number of four L7/L12 could have evolved to optimize sampling and pre-loading of ternary complexes under crowded conditions, and thus support faster overall growth. We encourage further work to explore the implications of this hypothesis in experiment, e.g., how L7/L12 copy number might be engineered in bacteria to tune maximum growth rate.

MATERIALS AND METHODS

Computational Model

We constructed computational representations of 'translation voxels' of the *E. coli* cytoplasm (Fig. 1*A*) in the molecular dynamics package LAMMPS [32], following the initial model described in [3]. In this work, each periodically-replicated voxel contains approximately 200,000 nearly-hard colloidal spheres representing ribosomes (with radius $a_{\mathrm{rib}} = 13\,\mathrm{nm}$), ternary complexes ($a_{\mathrm{tern}} = 5.9\,\mathrm{nm}$), and other native cytoplasmic proteins ($a_{\mathrm{prot}} = 2\,\mathrm{nm}$). The abundance of each molecule (N_i), voxel length (l_{vox}), and total voxel volume fraction (ϕ_{tot}) depend on cellular growth rate (Table S1). Please see [3] for a detailed description of how voxel parameters were obtained from experimental measurements.

A pair of molecules i and j can interact in translation voxels via entropic or attractive components, defined by the potential:

$$\frac{V\left(r_{ij}\right)}{k_{\mathrm{B}}T} = \begin{cases} V_{\mathrm{rep}} = 6\left(1 - e^{-60\left(r_{ij}-\sigma_{ij}\right)}\right)^2 - \varepsilon_{ij} & \text{if } r_{ij} \leq \sigma_{ij} \\ V_{\mathrm{attr}} = -\varepsilon_{ij}\sigma_{ij}/r_{ij}e^{-z\left(r_{ij}/\sigma_{ij}-1\right)} & \text{if } r_{ij} > \sigma_{ij}, \end{cases} \tag{1}$$

where r_{ij} is the magnitude of the unit vector $\hat{\boldsymbol{r}}_{ij}$ pointing from the center of particle j to the center of particle i, k_{B} is the Boltzmann constant, and T is the absolute temperature. Entropic exclusion is enforced via a Morse potential, V_{rep}, previously demonstrated to recover hard-sphere behavior [22]. The hard-sphere contact distance σ_{ij} is defined as the sum of particle radii, a_i and a_j.

Previous structural homology-based and kinetic experiments suggest that the EF-Tu·L7/L12 interaction consists of a hydrophobic patch flanked by two salt bridges [12, 13]. To capture the exponential character of such interactions [33, 34], we represented the attraction between ternary complexes and ribosomes via a Yukawa potential, V_{attr}. The attraction range of hydrophobic interactions and salt bridges (approximately $0.4\,\mathrm{nm}$ [34, 35]) corresponds with a decay rate constant $z = 10/\sigma_{ij}$ in Eq. . The characteristic attraction strength, ε_{ij}, sets the depth of the potential well. We estimated the *in vivo* attraction strength to be $\varepsilon_{\mathrm{t,r}}^{\mathrm{exp}} = 16\,k_{\mathrm{B}}T$, assuming each salt bridge contributes $3\,\mathrm{kcal/mol}$ ($4.9\,k_{\mathrm{B}}T$ at 37^oC, [36]) and the hydrophobic patch contributes $4\,\mathrm{kcal/mol}$ ($6.5\,k_{\mathrm{B}}T$ at 37^oC). To calculate the hydrophobic contribution, we assumed that a $18\,\mathrm{cal\,mol}^{-1-2}$ free energy density [37] is distributed over a hemisphere of diameter 11.8 , the size of the hydrophobic region of the L7/L12 C-terminal domain (PDB code ICTF [38]). We also investigated weaker isotropic attraction strengths of $\varepsilon_{\mathrm{t,r}} = 3\,k_{\mathrm{B}}T$ and $6\,k_{\mathrm{B}}T$, which have been demonstrated to drive formation

of phase-separated droplets [39] and arrested gel networks [23], respectively. Interactions between other types of molecules are purely repulsive at contact and otherwise do not interact, i.e., $\varepsilon_{ij\neq \mathrm{t,r}} = 0$.

To build a limited-valency interaction model, we first calculated the ribosome surface area accessible to the highly mobile L7/L12 subunits. Using the structural model from [14], we projected the range of movement of all four L7/L12 subunits onto a ribosome body of size $a_{\mathrm{rib}} = 13\,\mathrm{nm}$ (Fig. 5*A*). The resulting spherical cap with base radius $h = 0.61\,a_{\mathrm{rib}}$ has a surface area $A_{\mathrm{cap}} = 220.4\,\mathrm{nm}^2$, approximately 11% of the total ribosome surface area $A_{\mathrm{rib}} = 2123.7\,\mathrm{nm}^2$. We embedded four spheres representing the L7/L12 subunits at evenly spaced intervals around the boundary of this accessible surface area. These spheres were inset to expose small binding site caps with base radii $b = 1.2\,\mathrm{nm}$, the measured size of the L7/L12 C-terminal domain (PDB code ICTF [38]). All measurements of structural models in this work were conducted using UCSF ChimeraX [40]. We embedded an identical inset sphere in the surface of each ternary complex to represent the equivalent binding site on EF-Tu (Fig. 5*A*). In the limited-valency model, the Yukawa attraction V_{attr} (Eq. 1) is only felt between these inset binding sites representing the EF-Tu and L7/L12 domains.

To interrogate a range of L7/L12 copy numbers, c, we modeled ribosomes with two, six, and eight binding sites of identical size to the previously described $c = 4$ model. For $c = 2$, we inset the binding sites on opposite sides of the L7/L12 accessible surface area (Fig. 5*A*, 7*A*). For $c = 6$ and $c = 8$, we inset one binding site at the center and five and seven binding sites, respectively, equally spaced around the circumference of the L7/12 accessible surface area. When $c \geq 6$, we expanded the accessible surface area to maintain the same binding site spacing as in the $c = 4$ case to prevent a single ternary complex from binding to multiple L7/L12 at a time.

Dynamic Simulation Method

Molecules are immersed in an implicit Newtonian solvent with viscosity $\eta = 0.6913\,\mathrm{mPa/s}$ and density $\rho = 0.99336\,\mathrm{g/cm}^3$, chosen to represent water at $37^o\,\mathrm{C}$. The small size of translation molecules sets a vanishingly small Reynolds number, $Re = \rho U a_i/\eta$, where U is the characteristic particle velocity. Fluid motion is thus governed by Stokes' equations, whereas particle motion is governed by the Langevin equation [41]:

$$\boldsymbol{m} \cdot \frac{d\boldsymbol{U}}{dt} = \boldsymbol{F}^{\mathrm{H}} + \boldsymbol{F}^{\mathrm{B}} + \boldsymbol{F}^{\mathrm{P}}, \tag{2}$$

where $\boldsymbol{m}$ is the mass tensor and $\boldsymbol{U}$ is the particle velocity. $\boldsymbol{F}^{\mathrm{H}}$ is the hydrodynamic force on each particle i given by Stokes drag law $\boldsymbol{F}_i^{\mathrm{H}} = -6\pi\eta a_i\,[\boldsymbol{U}_i - \langle \boldsymbol{u} \rangle]$, where $\langle \boldsymbol{u} \rangle$ is the bulk fluid velocity, which is zero for a quiescent prokaryotic cytoplasm. The stochastic Brownian force $\boldsymbol{F}^{\mathrm{B}}$ emerges from thermal solvent fluctuations and obeys Gaussian statistics:

$$\boldsymbol{F}_i^{\mathrm{B}} = 0,\ \overline{\boldsymbol{F}_i^{\mathrm{B}}(0)\boldsymbol{F}_i^{\mathrm{B}}(t)} = 2k_{\mathrm{B}}T(6\pi\eta a_i)\boldsymbol{I}\delta(t), \tag{3}$$

where overbars indicate averages over long times compared to the solvent timescale, $\boldsymbol{I}$ is the identity tensor, and $\delta(t)$ is the Dirac delta function. The deterministic interparticle force $\boldsymbol{F}^{\mathrm{P}}$ is the gradient of the interaction potential V_{ij} between a particle pair (Eq. 1):

$$\boldsymbol{F}_i^{\mathrm{P}} = -\sum_j \frac{\partial V_{ij}(r_{ij})}{\partial r_{ij}} \hat{\boldsymbol{r}}_{ij}. \tag{4}$$

We instantiated the initial distribution of finite sized molecules in translation voxels using PACKMOL [42]. In LAMMPS, Eq. 2 is integrated forward in time using the velocity-Verlet method [43] and a Langevin thermostat [44] to solve for particle trajectories. We chose a sufficiently small discretization timestep, $\Delta t = 13\,\mathrm{ps}$, and damping factor, $d = 0.01$, to recover the inertia-less physics of the Stokes flow regime [22]. In the limited-valency model, each ribosome and ternary complex with inset binding sites is treated as a rigid body using the 'fix rigid' command in LAMMPS. Simulations were evolved for $1.3\,\mathrm{ms}$, with full particle trajectories output every $130\,\mathrm{ns}$. Visualizations of simulations were created using Visual Molecular Dynamics (VMD, [45]).

Suspension Microstructure

We calculated the radial distribution function, $g(r)$, to characterize pair-level correlations between ternary complexes and ribosomes, defined according to [46, 47]

$$g(r) = \frac{V_{\mathrm{tot}}}{N_{\mathrm{rib}} N_{\mathrm{tern}}} \left\langle \sum_{i=1}^{N_{\mathrm{rib}}} \sum_{j=1}^{N_{\mathrm{tern}}} \delta\left(\boldsymbol{r} + \boldsymbol{r}_i - \boldsymbol{r}_j\right) \right\rangle, \tag{5}$$

where $V_{\mathrm{tot}} = (l_{\mathrm{vox}})^3$ is the total voxel volume and the function $\sum_{i=1}^{N_{\mathrm{rib}}} \sum_{j=1}^{N_{\mathrm{tern}}} \delta\left(\boldsymbol{r} + \boldsymbol{r}_i - \boldsymbol{r}_j\right)$ is the microscopic particle density at a given position $\boldsymbol{r}$, calculated in translation voxels with separations $\boldsymbol{r}_i - \boldsymbol{r}_j$ for all i ribosome and j ternary complex pairs. The radial distribution function is normalized to reflect departures from a uniform distribution, $g(r) = 1$ that arise from finite size and other effects.

We calculated the static structure factor $S(\boldsymbol{q})$, the wave-space equivalent of $g(r)$ that is typically obtained in scattering experiments [23, 46] according to:

$$S(\boldsymbol{q}) = \frac{1}{N} \sum_{k=1}^{N} \sum_{l=1}^{N} e^{-i\boldsymbol{q}\cdot(\boldsymbol{r}_k - \boldsymbol{r}_l)}, \tag{6}$$

where $\boldsymbol{q}$ is the wavevector normalized by the ribosome size a_{rib}, N is the number of particles, and $\boldsymbol{r}_k - \boldsymbol{r}_l$ is the separation for a particle pair (k, l). $S(\boldsymbol{q})$ is radially averaged to give $S(q)$, where $q = |\boldsymbol{q}|$ and corresponds to a real space length of $l = 2\pi/q$. We are interested in quantifying long-range correlations throughout the translation voxel and thus calculated $S(q)$ for all particles $N = N_{\mathrm{rib}} + N_{\mathrm{tern}} + N_{\mathrm{prot}}$ in the ensemble.

Dynamics and Rheology

We monitored dynamics by tracking particle positions throughout simulation and computing their mean-square displacement (MSD) over time

$$\mathrm{MSD}_i = \langle \Delta\boldsymbol{x}_i \Delta\boldsymbol{x}_i \rangle, \tag{7}$$

where $\Delta\boldsymbol{x} = \boldsymbol{x}(t) - \boldsymbol{x}(0)$ is the change in particle position from the initial time to the current time t, and i is the particular molecular species (ribosome, ternary complex, or small native protein). Angle brackets denote an ensemble average over all molecules of that species. We extracted the long-time self-diffusivity, $D^s_{\infty,i}$ for each species from the slope of the MSD over long times

$$D^s_{\infty,i} = \frac{1}{6} \frac{d\left(\mathrm{MSD}_i\right)}{dt}\bigg|_{t = 0.4 - 0.6\,\mathrm{ms}}. \tag{8}$$

Cellular confinement and the presence of hydrodynamic interactions are expected to slow diffusion *in vivo*. Thus, to compare dynamics in our freely-draining, unconfined model to experimental measurements, we scaled $D^s_{\infty,i}$ by a volume fraction dependent factor which accounts for both confinement and hydrodynamic effects. We derived this scaling factor using analytical theory [48, 49] and results from confined Brownian and Stokesian Dynamics simulations [50, 51]. Details can be found in the *SI Appendix* and Fig. S1.

We used this molecular diffusivity to calculate the effective cytoplasmic viscosity experienced by ternary complexes $\eta_{\mathrm{eff,tern}}$, given by the Stokes-Einstein relation [52, 53], which is a reasonable approximation in concentrated suspensions if the produced viscosity is interpreted as a microscopic rather than a bulk viscosity [54]:

$$\eta_{\mathrm{eff,tern}} = \frac{k_{\mathrm{B}} T}{6\pi a_{\mathrm{tern}} D^s_{\infty,\mathrm{tern}}}, \tag{9}$$

Here, $D^s_{\infty,\mathrm{tern}}$ is the scaled long-time self-diffusivity, accounting for hydrodynamic and confinement effects (*SI Appendix*, Fig. S1). We normalized this effective viscosity by that of water at $37^o\,C$, $\eta_0 = 0.6913\,\mathrm{cP}$, to capture the entropic contribution due to finite molecular size.

Binding Metrics

To quantify co-localization of the translation machinery, we calculated the fraction of ribosome-bound ternary complexes, f, in each voxel:

$$f = \frac{N_{\mathrm{tern,bound}}}{N_{\mathrm{tern,tot}}} \tag{10}$$

where $N_{\mathrm{tern,tot}}$ is the total number and $N_{\mathrm{tern,bound}}$ is the ribosome-bound number of ternary complexes. A ternary complex, i, is considered bound to a ribosome, j, if their center-to-center separation r_{ij} is less than the maximum bond distance $r_{\mathrm{cut}} = 21\,\mathrm{nm}$ (for details, see *SI Appendix* and Fig. S12). This bound fraction was estimated *in vivo* by Mustafi and Weisshaar to be $f_{\mathrm{exp}} = 0.6$ at a growth rate of 1 dbl/hr [17]. In the *SI Appendix* (Fig. S10), we describe in detail how we extrapolated this experimental measurement to higher growth rates by accounting for changes in molecular stoichiometry and crowding.

We calculated the apparent binding affinity of the interaction between ribosomes and ternary complexes, as defined in [55]:

$$K_{\mathrm{d,app}} = n\,[R]_{\mathrm{tot}}\,\frac{[T]_{\mathrm{free}}}{[T]_{\mathrm{bound}}} - [T]_{\mathrm{free}}\,, \tag{11}$$

where we assume each ribosome has n independent sites to which ternary complexes can bind. $[R]_{\mathrm{tot}}$ is the total concentration of ribosomes, and $[T]_{\mathrm{free}}$ and $[T]_{\mathrm{bound}}$ are the concentrations of free and bound ternary complexes, respectively. Ribosome-bound ternary complexes are defined as in Eq. 10, i.e., if they are found within r_{cut} of a ribosome. For the case with isotropic attractions, the number of independent binding sites n is set by the number of ternary complexes that can fit around a ribosome at maximum packing. With a relative particle size ratio of $a_{\mathrm{tern}}/a_{\mathrm{rib}} = 0.45$, the isotropic number of binding sites is thus $n_{\mathrm{iso}} = 32$ [56]. For the limited-valency attraction case, we set the number of binding sites $n_{\mathrm{lim}} = 5$ to reflect the maximum measured coordination number of ribosomes, N_{c} (see *SI Appendix*, Fig. S11)

Binding Times and Sampling Rates

We quantified the duration of individual binding events by computing the time that ternary complexes spend within the maximum bond distance r_{cut} of a ribosome. According to this binding definition, we tracked the state of each ternary complex as 'bound' or 'unbound' over the $1.3\,\mathrm{ms}$ simulation evolution. If a ternary complex departed a bound state, the duration of that event was recorded in the distribution of binding times. The identity of that ternary complex was also recorded as having been 'sampled' by that ribosome. At the end of the analysis window, we computed the number of unique ternary complexes that each ribosome sampled, normalized by the maximum number sampled in the $c = 2$ case. We visualized the probability distributions of binding event durations and sampling fractions using the Python Seaborn package for kernel density estimates.

We quantified the tradeoff between co-localization and mobility by the product of the fractions of bound, f, and freely diffusing ternary complexes, $(1 - f)$. Without scaling, this product would be maximized at $f = 0.5$, whereas $f^{\textit{in vivo}} = 0.67$ at a growth rate of 3 dbl/hr (Fig. 5*D*). To account for this favoring of the bound state *in vivo*, we raised the bound fraction f to a power $\alpha = 1.71$, corresponding to the difference in energies $(\varepsilon_{\mathrm{free}} - \varepsilon_{\mathrm{bound}})$ in a two-state Boltzmann distribution [57]:

$$\frac{p_{\mathrm{bound}}}{p_{\mathrm{free}}} = e^{\varepsilon_{\mathrm{free}} - \varepsilon_{\mathrm{bound}}} \tag{12}$$

where $p_{\mathrm{bound}} = f^{\textit{in vivo}}$ and $p_{\mathrm{free}} = 1 - f^{\textit{in vivo}}$.

Modeling Chemical Reactions and Elongation Latencies

To simulate the coupled physics and chemistry of translation elongation, we developed a bespoke version of LAMMPS [32] that allows for changes to interparticle interactions based on distance, time, and particle type. In each translation voxel simulation ($N_{\mathrm{sim}} = 1,170$ per growth rate), we randomly picked a ribosome to track and classified all ternary complexes as either cognates or non-cognates based on the physiological distribution of codon and tRNA abundances, following the framework developed in [3]. To represent codon-anticodon testing, we modified our limited-valency interaction model to include internal sites within each ribosome and ternary complex, representing the A-site codon and tRNA anti-codon, respectively (see *SI Appendix*, Fig. S15).

In simulation, we allowed particles to diffuse and interact as in the physics-only model described above. To simulate the initial aa-tRNA recognition test, we used a distance-based rule to change the pairwise interactions between ribosomes and ternary complexes that are in close physical proximity. Namely, if the center-to-center distance between L7/L12 and EF-Tu sites is less than 1.05 times their hard-sphere contact distance (i.e., $2.52\,\mathrm{nm}$), we considered their respective ribosome and ternary complex as having begun reacting. We note that molecules can only be involved in one reaction at a time. To simulate the entry of a captured ternary complex into the ribosome, we turned off the hard sphere repulsion between reacting pairs, and turn on a $16\,k_{\mathrm{B}}T$ attraction between their internal A-site codons and tRNA anti-codons (see *SI Appendix*, Fig. S15). The duration of each reaction was drawn from a latency distribution derived from experimental kinetic rates [3], depending on if the codon and anticodon are cognates or non-cognates (see *SI Appendix*, Fig. S13). We accounted for the presence of near-cognate ternary complexes by randomly scaling non-cognate reaction durations by 3.3-fold with a 20% probability, as in [3]. If the reaction is not successful, the simulation was allowed to proceed for the sampled reaction duration, before ternary complex release was imposed by a soft repulsion between the reacting pair. Once the center-to-center distance is above a distance threshold ($12.2\,\mathrm{nm}$), both particles in the simulation are returned to the non-reacting pool and can start another reaction upon their next encounter. When a successful cognate match is found, the simulation is terminated.

The previous reaction framework [3] scaled physiological kinetic rates by 600-fold, which enabled computational tractability while maintaining a well-mixed distribution of particles within simulation. Since physical binding events in our limited-valency model last ten times longer on average than in non-attractive voxels, we scaled kinetic rates here by only 60-fold. See a detailed discussion of this speedup in [3], particularly the section "Acceleration of translation voxel simulations to reduce run time and cost."

For each growth rate, we calculated a reaction latency ($\overline{\tau}_{\mathrm{rxn}}$), defined as the time the cognate ternary complex spends in reactions; an elongation latency ($\overline{\tau}_{\mathrm{elong}}$), defined as the total time the matching ribosome spends unbound or in reactions; and a transport latency ($\overline{\tau}_{\mathrm{transport}}$), calculated as the difference between the elongation and reaction latency. We followed the method described in detail in [3], including the impacts of physiological variability in cognate abundances.

Prokaryotic L7/L12 Copy Number

L7/L12 copy number, c, has been quantified for more than $1,200$ bacteria, mitochondria, and chloroplasts by computational analysis and mass spectrometry [29]. We focused on a subset of $N = 354$ bacteria across five phyla for which minimal doubling times are also known (Table S2), gathered from the '$\mathrm{condensed_traits_NCBI.csv}$' supplementary file of [58] (`https://doi.org/10.6084/m9.figshare.12221732`). We separated this subset into three populations of size N_c according to L7/L12 copy number, where $N_4 = 149$, $N_6 = 182$, and $N_8 = 23$. We then visualized the probability distribution of minimal doubling times for each population using the Python Seaborn package for kernel density estimates. We compared the means of the distributions via the Mann-Whitney U-test in SciPy, with $p < 0.001$ for all cases.

ACKNOWLEDGMENTS

We thank Drew Endy, Akshay Maheshwari, and Emma Gonzalez for insightful discussions regarding the initial translation voxel model. This work was supported by National Science Foundation Graduate Research Fellowships under Grant No. 1656518 for J.L.H. and A.M.S., Stanford Graduate Fellowships for A.M.S and T.S.Y., and an ARCS Foundation Award for J.L.H..

Computing was performed on the Sherlock cluster at the Stanford Research Computing Center (SRCC) and on Stampede2 at the Texas Advanced Computing Center (TACC). SRCC resources were provided by Stanford University, while resources at TACC were supported by the National Science Foundation's Extreme Science and Engineering Discovery Environment (XSEDE) Research Award No. CTS130035 and Advanced Cyberinfrastructure Coordination Ecosystem: Services & Support (ACCESS) Research Award No. CHM230007.

AUTHOR CONTRIBUTIONS

J.L.H. and R.N.Z. designed research; J.L.H. and T.S.Y. performed research; J.L.H., T.S.Y., and A.M.S. analyzed data; and J.L.H., T.S.Y., A.M.S., and R.N.Z. wrote the paper.

AUTHOR COMPETING INTERESTS

The authors declare no competing interests

REFERENCES

[1] Ken A. Dill, Kingshuk Ghosh, and Jeremy D. Schmit. Physical limits of cells and proteomes. *Proceedings of the National Academy of Sciences of the United States of America*, 108:17876–17882, 11 2011.

[2] Nathan M. Belliveau, Griffin Chure, Christina L. Hueschen, Hernan G. Garcia, Jane Kondev, Daniel S. Fisher, Julie A. Theriot, and Rob Phillips. Fundamental limits on the rate of bacterial growth and their influence on proteomic composition. *Cell Systems*, 12:924–944.e2, 9 2021.

[3] Akshay J. Maheshwari, Alp M. Sunol, Emma Gonzalez, Drew Endy, and Roseanna N. Zia. Colloidal physics modeling reveals how per-ribosome productivity increases with growth rate in escherichia coli. *mBio*, 12 2022.
[4] Hans Bremer and Patrick P. Dennis. Modulation of chemical composition and other parameters of the cell at different exponential growth rates. *EcoSal Plus*, 3, 2 2008.
[5] Benjamin Volkmer and Matthias Heinemann. Condition-dependent cell volume and concentration of escherichia coli to facilitate data conversion for systems biology modeling. *PLOS ONE*, 6:e23126, 2011.
[6] Hengjiang Dong, Lars Nilsson, and Charles G. Kurland. Co-variation of trna abundance and codon usage in escherichia coli at different growth rates. *Journal of Molecular Biology*, 260:649–663, 8 1996.
[7] Steen Pedersen, Phillip L. Bloch, Solvejg Reeh, and Frederick C. Neidhardt. Patterns of protein synthesis in e. coli: a catalog of the amount of 140 individual proteins at different growth rates. *Cell*, 14:179–190, 5 1978.
[8] Alexander Schmidt, Karl Kochanowski, Silke Vedelaar, Erik Ahrné, Benjamin Volkmer, Luciano Callipo, Kèvin Knoops, Manuel Bauer, Ruedi Aebersold, and Matthias Heinemann. The quantitative and condition-dependent escherichia coli proteome. *Nature Biotechnology 2015 34:1*, 34:104–110, 1 2016.
[9] Conrad L Woldringh and Nanne Nanninga. Structure of nucleoid and cytoplasm of the intact cell, 1985.
[10] Stefan Klumpp, Matthew Scott, Steen Pedersen, and Terence Hwa. Molecular crowding limits translation and cell growth. *Proceedings of the National Academy of Sciences of the United States of America*, 110:16754–16759, 10 2013.
[11] Holger Stark, Marina V. Rodnina, Jutta Rinke-Appel, Richard Brimacombe, Wolfgang Wintermeyer, and Marin Van Heel. Visualization of elongation factor tu on the escherichia coli ribosome. *Nature 1997 389:6649*, 389:403–406, 1997.
[12] Hans Joachim Wieden, Wolfgang Wintermeyer, and Marina V. Rodnina. A common structural motif in elongation factor ts and ribosomal protein l7/12 may be involved in the interaction with elongation factor tu. *Journal of Molecular Evolution 2001 52:2*, 52:129–136, 2001.
[13] Ute Kothe, Hans Joachim Wieden, Dagmar Mohr, and Marina V. Rodnina. Interaction of helix d of elongation factor tu with helices 4 and 5 of protein l7/12 on the ribosome. *Journal of Molecular Biology*, 2004.
[14] Mihaela Diaconu, Ute Kothe, Frank Schlünzen, Niels Fischer, Jörg M. Harms, Alexander G. Tonevitsky, Holger Stark, Marina V. Rodnina, and Markus C. Wahl. Structural basis for the function of the ribosomal l7/12 stalk in factor binding and gtpase activation. *Cell*, 2005.
[15] Rebecca M. Voorhees and V. Ramakrishnan. Structural basis of the translational elongation cycle. *https://doi.org/10.1146/annurev-biochem-113009-092313*, 82:203–236, 6 2013.
[16] Anders Liljas and Suparna Sanyal. The enigmatic ribosomal stalk. *Quarterly reviews of biophysics*, 51:e12, 2018.
[17] Mainak Mustafi and James C. Weisshaar. Simultaneous binding of multiple ef-tu copies to translating ribosomes in live escherichia coli. *mBio*, 9, 1 2018.
[18] Akshay Maheshwari, Alp M Sunol, Emma Gonzalez, Drew Endy, and Roseanna N Zia. Perspective: Colloidal hydrodynamics of biological cells, A frontier for two fields. *Physical Review Fluids*, pages 1–42, 2019.
[19] D.S. Goodsell. Elongation factors. *RCSB Protein Data Bank*, 9 2006.
[20] D.S. Goodsell. Phytase. *RCSB Protein Data Bank*, sep 2018.
[21] Wojciech M. Smigiel, Luca Mantovanelli, Dmitrii S. Linnik, Michiel Punter, Jakob Silberberg, Limin Xiang, Ke Xu, and Bert Poolman. Protein diffusion in escherichia coli cytoplasm scales with the mass ofthe complexes and is location dependent. *Science Advances*, 8:5387, 8 2022.
[22] Roseanna N Zia, Benjamin J Landrum, and William B Russel. A micro-mechanical study of coarsening and rheology of colloidal gels: Cage building, cage hopping, and smoluchowski's ratchet. *Journal of Rheology*, 58:1121, 2014.
[23] Lilian C. Johnson, Roseanna N. Zia, Esmaeel Moghimi, and George Petekidis. Influence of structure on the linear response rheology of colloidal gels. *Journal of Rheology*, 63:583, 5 2019.
[24] Daria V Fedyukina, Theodore S Jennaro, and Silvia Cavagnero. Charge segregation and low hydrophobicity are key features of ribosomal proteins from different organisms. *Journal of Biological Chemistry*, 289, 2014.
[25] Dmitry Tworowski and Mark Safro. The long-range electrostatic interactions control trna-aminoacyl-trna synthetase complex formation. *Protein Science*, 12:1247–1251, 2003.
[26] Jeffrey F. Morris. A review of microstructure in concentrated suspensions and its implications for rheology and bulk flow. *Rheologica Acta*, 48:909–923, 3 2009.
[27] W. B. Russel, D. A. Saville, and W. R. Schowalter. *Colloidal Dispersions*. Cambridge University Press, 12 1989.
[28] Jake L. Weissman, Shengwei Hou, and Jed A. Fuhrman. Estimating maximal microbial growth rates from cultures, metagenomes, and single cells via codon usage patterns. *Proc. Natl. Acad. Sci. U. S. A.*, 118(12), mar 2021.
[29] Iakov I. Davydov, Ingo Wohlgemuth, Irena I. Artamonova, Henning Urlaub, Alexander G. Tonevitsky, and Marina V. Rodnina. Evolution of the protein stoichiometry in the L12 stalk of bacterial and organellar ribosomes. *Nat. Commun.*, 4, 2013.
[30] Chandra Sekhar Mandava, Kristin Peisker, Josefine Ederth, Ranjeet Kumar, Xueliang Ge, Witold Szaflarski, and Suparna Sanyal. Bacterial ribosome requires multiple L12 dimers for efficient initiation and elongation of protein synthesis involving IF2 and EF-G. *Nucleic Acids Res.*, 40(5):2054–2064, mar 2012.
[31] H. J. Grosjean, S. De Henau, and D. M. Crothers. On the physical basis for ambiguity in genetic coding interactions. *Proc. Natl. Acad. Sci.*, 75(2):610–614, feb 1978.
[32] Aidan P. Thompson, H. Metin Aktulga, Richard Berger, Dan S. Bolintineanu, W. Michael Brown, Paul S. Crozier, Pieter J. in 't Veld, Axel Kohlmeyer, Stan G. Moore, Trung Dac Nguyen, Ray Shan, Mark J. Stevens, Julien Tranchida, Christian Trott, and Steven J. Plimpton. Lammps - a flexible simulation tool for particle-based materials modeling at the atomic, meso, and continuum scales. *Computer Physics Communications*, 271:108171, 2 2022.
[33] Jan Spitzer and Bert Poolman. The role of biomacromolecular crowding, ionic strength, and physicochemical gradients in the complexities of life's emergence. *Microbiology and Molecular Biology Reviews*, 73:371–388, 2009.
[34] Rico F Tabor, Chu Wu, Franz Grieser, Raymond R Dagastine, and Derek Y C Chan. Measurement of the hydrophobic force in a soft matter system. *J. Phys. Chem. Lett*, 4:3877, 2013.
[35] Benjamin Folch, Marianne Rooman, and Yves Dehouck. Thermostability of salt bridges versus hydrophobic interactions in proteins probed by statistical potentials. *J. Chem. Inf. Model.*, 48:119–127, 2008.
[36] D. Eric Anderson, Wayne J. Becktel, and F. W. Dahlquist. ph-induced denaturation of proteins: A single salt bridge contributes 3-5 kcal/mol to the free energy of folding of t4 lysozyme. *Biochemistry*, 29:2403–2408, 3 1990.
[37] Liguo Jiang, Siqin Cao, Peter Pak Hang Cheung, Xiaoyan Zheng, Chris Wai Tung Leung, Qian Peng, Zhigang Shuai, Ben Zhong Tang, Shuhuai Yao, and Xuhui Huang. Real-time monitoring of hydrophobic aggregation reveals a critical role of cooperativity in hydrophobic effect. *Nature Communications 2017 8:1*, 8:1–8, 5 2017.
[38] Marie Leijonmarck and Anders Liljas. Structure of the c-terminal domain of the ribosomal protein l7l12 from escherichia coli at 1.7 å. *Journal of Molecular Biology*, 195:555–579, 6 1987.
[39] Jennifer L. Hofmann, Akshay J. Maheshwari, Alp M. Sunol, Drew Endy, and Roseanna N. Zia. Ultra-weak protein-protein interactions can modulate proteome-wide searching and binding. *bioRxiv*, page 2022.09.30.510365, 10 2022.
[40] Eric F. Pettersen, Thomas D. Goddard, Conrad C. Huang, Elaine C. Meng, Gregory S. Couch, Tristan I. Croll, John H. Morris, and Thomas E. Ferrin. Ucsf chimerax: Structure visualization for researchers, educators, and developers. *Protein Science*, 30:70–82, 1 2021.
[41] Paul Langevin. Sur la theorie du mouvement brownien. *Comptes-rendus de l'Académie des sciences*, 146:530–533, 1908.
[42] L. Martinez, R. Andrade, E. G. Birgin, and J. M. Martínez. PACKMOL: A package for building initial configurations for molecular dynamics simulations. *J. Comput. Chem.*, 30(13):2157–2164, oct 2009.
[43] Michael P. Allen and Dominic J. Tildesley. *Computer Simulation of Liquids*. Oxford University Press, 2nd editio edition, 11 2017.
[44] Axel Brünger, Charles L. Brooks, and Martin Karplus. Stochastic boundary conditions for molecular dynamics simulations of st2 water. *Chemical Physics Letters*, 105:495–500, 3 1984.
[45] William Humphrey, Andrew Dalke, and Klaus Schulten. Vmd: Visual molecular dynamics. *Journal of Molecular Graphics*, 14:33–38, 2 1996.
[46] Jean Pierre Hansen and Ian R. McDonald. *Theory of simple liquids*. Elsevier Academic Press, 3rd ed. edition, 2006.
[47] Alice L. Thorneywork, Roland Roth, Dirk G.A.L. Aarts, and Roel P.A. Dullens. Communication: Radial distribution functions in a two-dimensional binary colloidal hard sphere system. *The Journal of Chemical Physics*, 140:161106, 4 2014.
[48] C.W.J Beenakker and P. Mazur. Diffusion of spheres in a concentrated suspension ii. *Physica*, 126A, 1984.
[49] John F. Brady. The long-time self-diffusivity in concentrated colloidal dispersions. *Journal of Fluid Mechanics*, 272:109–134, 1994.
[50] Christian Aponte-Rivera, Yu Su, and Roseanna N. Zia. Equilibrium structure and diffusion in concentrated hydrodynamically interacting suspensions confined by a spherical cavity. *Journal of Fluid Mechanics*, 836:413–450, 2 2018.
[51] Alp M. Sunol and Roseanna N. Zia. Confined Brownian suspensions: Equilibrium diffusion, thermodynamics, and rheology. *J. Rheol. (N. Y. N. Y).*, 67(2):433, jan 2023.
[52] George Gabriel Stokes. On the effect of the internal friction of fluids on the motion of pendulums. *Transactions of the Cambridge Philosophical Society*, 9, 1851.
[53] A. Einstein. Über die von der molekularkinetischen theorie der wärme geforderte bewegung von in ruhenden flüssigkeiten suspendierten teilchen. *Annalen der Physik*, 322:549–560, 1 1905.
[54] Roseanna N Zia. Active and Passive Microrheology: Theory and Simulation. *Annu. Rev. Fluid Mech*, 50:371–405, 2018.
[55] Hans Bisswanger. Multiple Equilibria, Principles, and Derivations. In *Enzym. Kinet.*, pages 1–26. John Wiley & Sons, Ltd, jun 2017.
[56] B W Clare and D L Kepert. The closest packing of equal circles on a sphere. *Proc. R. Soc. London. A. Math. Phys. Sci.*, 405(1829):329–344, jun 1986.
[57] Donald A McQuarrie. *Statistical mechanics*. Harper & Row, New York, 1976.
[58] Joshua S. Madin, Daniel A. Nielsen, Maria Brbic, Ross Corkrey, David Danko, Kyle Edwards, Martin K.M. Engqvist, Noah Fierer, Jemma L. Geoghegan, Michael Gillings, Nikos C. Kyrpides, Elena Litchman, Christopher E. Mason, Lisa Moore, Søren L. Nielsen, Ian T. Paulsen, Nathan D. Price, T. B.K. Reddy, Matthew A. Richards, Eduardo P.C. Rocha, Thomas M. Schmidt, Heba Shaaban, Maulik Shukla, Fran Supek, Sasha G. Tetu, Sara Vieira-Silva, Alice R. Wattam, David A. Westfall, and Mark Westoby. A synthesis of bacterial and archaeal phenotypic trait data. *Sci. Data 2020 7:1*, 7(1):1–8, jun 2020.
[59] Jerome K. Percus and George J. Yevick. Analysis of Classical Statistical Mechanics by Means of Collective Coordinates. *Phys. Rev.*, 110(1):1, apr 1958.
[60] W R Smith, D J Henderson, P J Leonard, J A Barker, and E W Grundke. Fortran codes for the correlation functions of hard sphere fluids. *Mol. Phys.*, 106(1):3–7, 2008.
[61] Loup Verlet and Jean Jacques Weis. Equilibrium Theory of Simple Liquids. *Phys. Rev. A*, 5(2):939, feb 1972.
[62] E. W. Grundke and D. Henderson. Distribution functions of multi-component fluid mixtures of hard spheres. *Mol. Phys.*, 24(2):269–281, aug 2006.

SI APPENDIX

Supplementary methods

Rescaling of diffusivity: confinement and hydrodynamics

To compare the long-time self-diffusivities D^s_∞ calculated in our simulations to those from *in vivo* particle tracking experiments [21], we derived a volume fraction dependent scaling factor to account for the effects of hydrodynamic interactions (HI) and confinement. The long-time self-diffusivity, D^s_∞, of a suspension of purely-repulsive hard spheres can be expressed [49] as:

$$D^s_\infty = D^s_0 \left[1 + 2\phi g(2,\phi)\right]^{-1}, \tag{S1}$$

where D^s_0 is the short-time self-diffusivity, ϕ is the volume fraction, and $g(2,\phi)$ is the value of the radial distribution function at contact for a given volume fraction ϕ. Our simulations represent the unbound freely-draining limit in which D^s_0 is simply D_0, the Stokes-Einstein equation of a single colloid diffusing in a continuum liquid [52, 53]. Thus,

$$\left.\frac{D^s_\infty}{D_0}\right|_{\mathrm{unb}} = \left[1 + 2\phi g(2,\phi)\right]^{-1}, \tag{S2}$$

holds in the unbound, freely-draining limit (solid black line, Fig. S1A). The analytical form of D^s_0 calculated by Beenakker and Mazur in 1984 [48] gives:

$$\left.\frac{D^s_\infty}{D_0}\right|_{\mathrm{unb,HI}} = \left(1 - 1.73\phi + 0.88\phi^2\right)\left[1 + 2\phi g(2,\phi)\right]^{-1}, \tag{S3}$$

for the unbound case with full HI (solid red line, Fig. S1A). Analogous analytical forms of D^s_0 do not yet exist for confined suspensions, so we turned to results from dynamic simulations. The confined D^s_0 are calculated from confined Brownian (dashed black line, Fig. S1A; freely-draining limit [51]) and Stokesian Dynamics simulations (dashed red line, Fig. S1A; with HI [50]), averaged over all positions in a spherical cavity with a confinement ratio of $\lambda_{\mathrm{c}} = a_{\mathrm{p}}/a_{\mathrm{cav}}$, where a_{p} and a_{cav} are the radii of the particle and cavity, respectively. In all cases, $g(2,\phi)$ was calculated via Percus-Yevick theory, as described in the subsequent section.

The volume fraction dependent scaling factor, s, is determined by the ratio of D^s_∞/D_0 for the unbound case and confined case with HI. The scaling factor increases with volume fraction (Fig. S1B), as crowding compounds the slow-down in diffusion from both hydrodynamic interactions and confinement. All instances of D^s_∞ in our work are divided by the value of $s(\phi)$, fit to a second-order polynomial in Python (Fig. S1B).

Theory for the bidisperse radial distribution function

We computed the radial distribution function $g(r)$ in translation voxels without small cytoplasmic proteins using Percus-Yevick (PY) theory [59]. We calculated $g(r)$ for bidisperse voxels using the code provided in [60] to numerically evaluate PY theory for hard sphere mixtures [61, 62] representing the size and abundance of ternary complexes and ribosomes across *E. coli* growth rates (Table S1). We examined two cases. First, we computed $g(r)$ when the total voxel volume V_{tot} is the same as in the tridisperse case, i.e., if crowders are simply removed (solid line, Fig. S5A). Second, we computed $g(r)$ when the total volume fraction ϕ_{tot} matches the tridisperse case, i.e., if crowders are removed and the voxel volume is reduced to recover the lost particle density (dashed line, Fig. S5B). To estimate the strength of this apparent depletion interaction, we ran dynamic simulations of bidisperse voxels across all *E. coli* growth rates, with volumes V_{tot} matching the tridisperse case. We included a $\varepsilon_{\mathrm{t,r}} = 1\,k_{\mathrm{B}}T$ attraction between ternary complexes and ribosomes (of the form in Eq. 1, Fig. 1C) and calculated $g(r)$ as described above via Eq. 5.

Coordination numbers

A ternary complex, i, is considered 'coordinated' with or bound to a ribosome, j, if their center-to-center separation r_{ij} is less than the maximum bond distance $r_{\mathrm{cut}} = 21$ nm. This value corresponds to a separation of 2.1 nm beyond hard-sphere contact, which includes the radii of the binding site protrusions and the width of the attractive well. According to this definition, we calculated the number of ternary complexes to which each ribosome is bound – its coordination number, N_{c}. We computed the distribution of ribosome coordination numbers for voxels across all growth rates and attraction strengths (Fig. S6, S11). We quantified the duration of individual binding events by computing the time that ternary complexes spend within the maximum bond distance r_{cut} of a ribosome (Fig. S12A).

Extrapolation of *in vivo* co-localization to faster growth rates

The fraction of ribosome-bound ternary complexes, f, has been measured *in vivo* at only one growth rate, $f^{\mathrm{exp}}(1\,\mathrm{dbl/hr}) = 0.6$. We extrapolated this *in vivo* measurement to faster cellular growth rates (Fig. S10) by calculating the expected change due to crowding ($+\Delta f_{\mathrm{crowd}}$) and stoichiometry ($+\Delta f_{\mathrm{stoich}}$). We defined the change in co-localization due to purely entropic forces as:

$$\Delta f_{\mathrm{crowd}}(\mathrm{gr}) = f^{\mathrm{iso,HS}}(\mathrm{gr}) - f^{\mathrm{iso,HS}}(1\,\mathrm{dbl/hr}) \tag{S4}$$

or the change in f with growth rate in the baseline hard sphere simulations (Fig. 4A, $\varepsilon_{\mathrm{t,r}} = 0\,k_{\mathrm{B}}T$. We define the change in co-localization due to stoichiometry as:

$$\Delta f_{\mathrm{stoich}}(\mathrm{gr}) = f^{\mathrm{max}}(\mathrm{gr}) - f^{\mathrm{max}}(1\,\mathrm{dbl/hr}) \tag{S5}$$

where $f^{\mathrm{max}}(\mathrm{gr}) = 4N_{\mathrm{rib}}(\mathrm{gr})/N_{\mathrm{tern}}(\mathrm{gr})$ is the maximum possible f, assuming that each ribosome is bound to exactly four ternary complexes. $N_{\mathrm{rib}}(\mathrm{gr})$ and $N_{\mathrm{tern}}(\mathrm{gr})$ were extracted and compiled from whole-cell measurements by [3]. We summed these two contributions ($+\Delta f_{\mathrm{tot}}$) to obtain the extrapolated *in vivo* bound fraction:

$$f^{\mathrm{exp}}(\mathrm{gr}) = f^{\mathrm{exp}}(1\,\mathrm{dbl/hr}) + \Delta f_{\mathrm{tot}}(\mathrm{gr}) \tag{S6}$$

Supplementary results

Static structure factor

We calculated the static structure factor, $S(q)$, in translation voxels across all *E. coli* growth rates and isotropic attraction strengths studied in this work (Fig. S2). In the hard sphere limit ($\varepsilon_{\mathrm{t,r}} = 0\,k_{\mathrm{B}}T$), we found that cytoplasmic polydispersity prevents the emergence of strong structural correlations at any wavevector q or real space length $l = 2\pi/q$. The probability of long-range correlations at small wavevectors is only slightly increased by weak isotropic attractions ($\varepsilon_{\mathrm{t,r}} = 3\,k_{\mathrm{B}}T$), suggesting the formation of transient low-order clusters. A single peak emerges for the $\varepsilon_{\mathrm{t,r}} = 6\,k_{\mathrm{B}}T$ attractive case, characteristic of a bicontinuous gel created by arrested phase separation. The peak shifts to higher wavevectors as crowding increases, corresponding with formation of thinner and shorter strands. In the $\varepsilon_{\mathrm{t,r}} = 16\,k_{\mathrm{B}}T$ attractive case, there is an abundance of correlations at longer length-scales (shorter wavevectors), but the stringier structure is not as well characterized by a single length-scale since ongoing phase separation is slowed by strong bonding [23].

Effective cytoplasmic viscosity

We calculated the effective cytoplasmic viscosity experienced by ternary complexes as a function of cellular growth rate, accounting for the impacts of hydrodynamic interactions and cellular confinement (see **Methods** above). Without attractions ($\varepsilon_{\mathrm{t,r}} = 0\,k_{\mathrm{B}}T$), the effective viscosity exhibits the expected increase with volume fraction, but underpredicts by two- to three-fold the *in vivo* estimate for equivalently-sized proteins in *E. coli* [21] (Fig. S3). Transient cluster formation in the case of weak isotropic attractions ($\varepsilon_{\mathrm{t,r}} = 3\,k_{\mathrm{B}}T$) drives an approximately 5% increase in effective viscosity, whereas stronger isotropic attractions over-predict *in vivo* viscosity by up to five-fold ($\varepsilon_{\mathrm{t,r}} = 6\,k_{\mathrm{B}}T$) and up to two orders of magnitude ($\varepsilon_{\mathrm{t,r}} = 16\,k_{\mathrm{B}}T$). In all cases, viscosity increases with cell growth rate as the cytoplasm densifies.

Supplementary tables

Table S1: Growth-rate dependent simulation parameters in translation voxels of *E. coli* cytoplasm

Doublings/hr	$\mu = 1.0$	$\mu = 1.5$	$\mu = 2.0$	$\mu = 2.5$	$\mu = 3.0$
N_{rib}	659	1,005	1,266	1,426	1,524
N_{tern}	3,528	4,662	6,090	7,476	8,820
N_{prot}	176,064	198,801	205,610	194,020	172,200
l_{vox}	405.0 nm	404.4 nm	403.7 nm	404.3 nm	404.0 nm
ϕ_{tot}	0.224	0.299	0.359	0.392	0.413

Supplementary figures

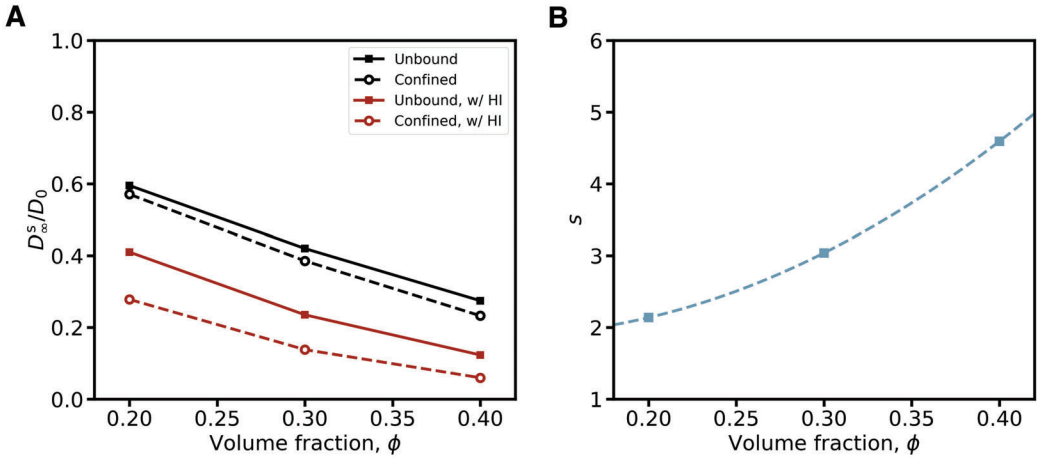

Figure S1: Hydrodynamic interactions and spherical confinement slow diffusion. (A) The long-time self-diffusivity, D^s_∞, normalized by the lone particle diffusivity, D_0, in a monodisperse hard sphere suspension, calculated as a function of volume fraction ϕ, the contact value of the radial distribution function g(r), and the short-time self-diffusivity D^s_0, as described in Supplementary Methods . The presence of both confinement (dashed lines) and hydrodynamic interactions (red lines) reduce the expected long-time self-diffusivity. **(B)** The scaling factor, s, is calculated via the ratio of D^s_∞ for the unbound and confined + HI cases (symbols), and is fit to a second-order polynomial across all volume fractions (dashed line).

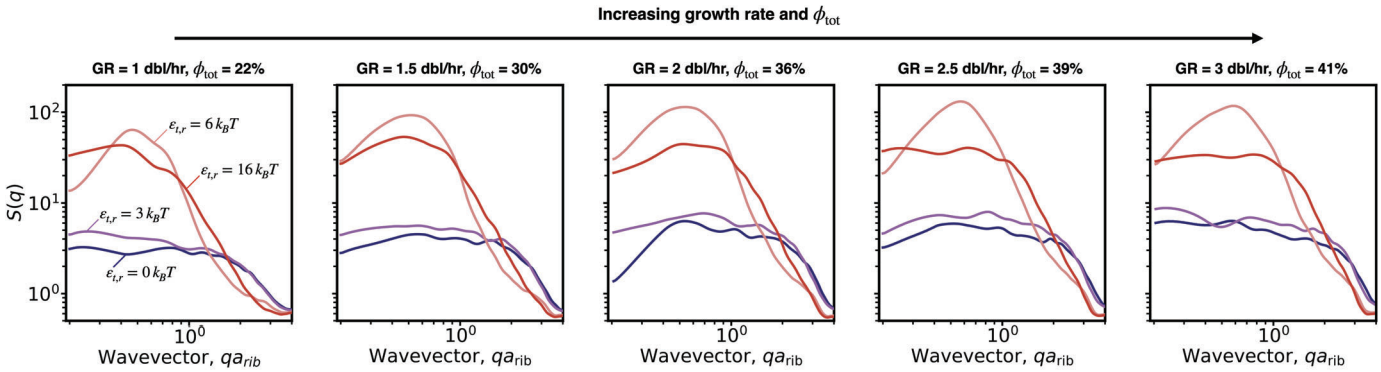

Figure S2: Structural length scales in the *E. coli* cytoplasm. Static structure factor, $S(q)$, as a function of cellular growth rate and overall volume fraction (left to right, marked at top), and strength of attractions between ternary complexes and ribosomes (colors, marked inset on left). The probability of long-range correlations at small wavevectors is only slightly increased by weak isotropic attractions ($\varepsilon_{\mathrm{t,r}} = 3\,k_{\mathrm{B}}T$), suggesting the formation of transient low-order clusters. A single peak emerges for the $\varepsilon_{\mathrm{t,r}} = 6\,k_{\mathrm{B}}T$ attractive case, characteristic of a bicontinuous gel created by arrested phase separation. In the $\varepsilon_{\mathrm{t,r}} = 16\,k_{\mathrm{B}}T$ attractive case, there is an abundance of correlations at longer length-scales (shorter wavevectors), but the stringier structure is not as well characterized by a single length-scale since ongoing phase separation is slowed by strong bonding [23].

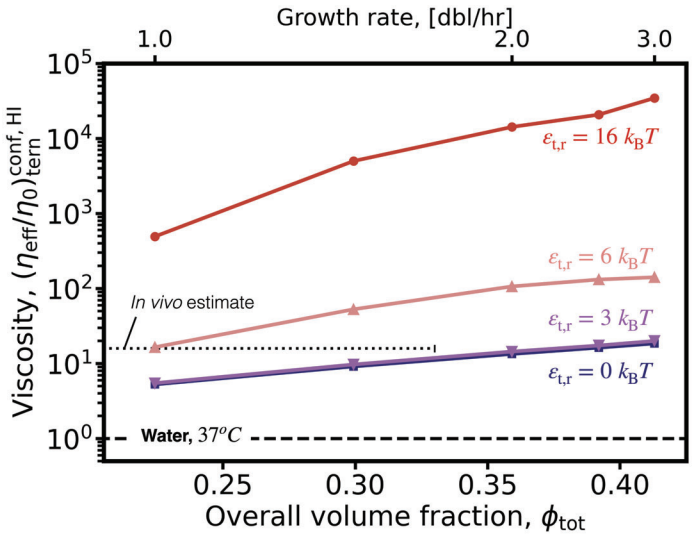

Figure S3: Arrest increases cytoplasmic viscosity beyond *in vivo* estimates. Effective cytoplasmic viscosity experienced by ternary complexes in translation voxels (Eq. 9), versus growth rate and volume fraction for all studied attraction strengths of $\varepsilon_{\text{t,r}} = 0\,k_{\text{B}}T$ (blue), $3\,k_{\text{B}}T$ (purple), $6\,k_{\text{B}}T$ (pink), and $16\,k_{\text{B}}T$ (red). The viscosity of water, η_0, at a temperature of $37^o\,C$ (horizontal dashed line) and the estimated *in vivo* viscosity experienced by a protein with a molecular weight of 69 kDa (M_{tern}) in *E. coli* (horizontal dotted line, [21]) are marked.

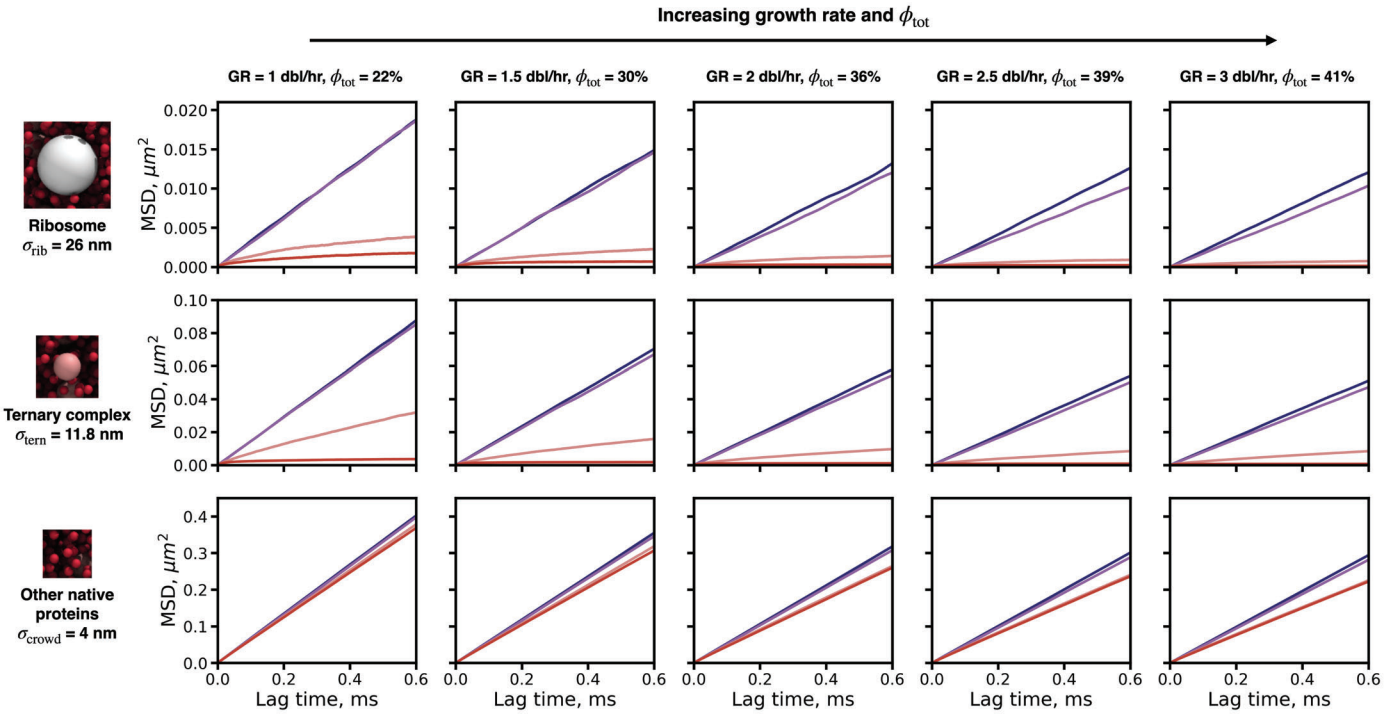

Figure S4: Dynamics of translation molecules are suppressed by increased crowding and attraction strength. Mean squared displacements versus lag time are plotted for ribosomes (top row), ternary complexes (middle row), and other native cytoplasmic proteins (bottom row), for each growth rate (left to right) and attraction strengths of $\varepsilon_{t,r} = 0\, k_B T$ (blue), $3\, k_B T$ (purple), $6\, k_B T$ (pink), and $16\, k_B T$ (red).

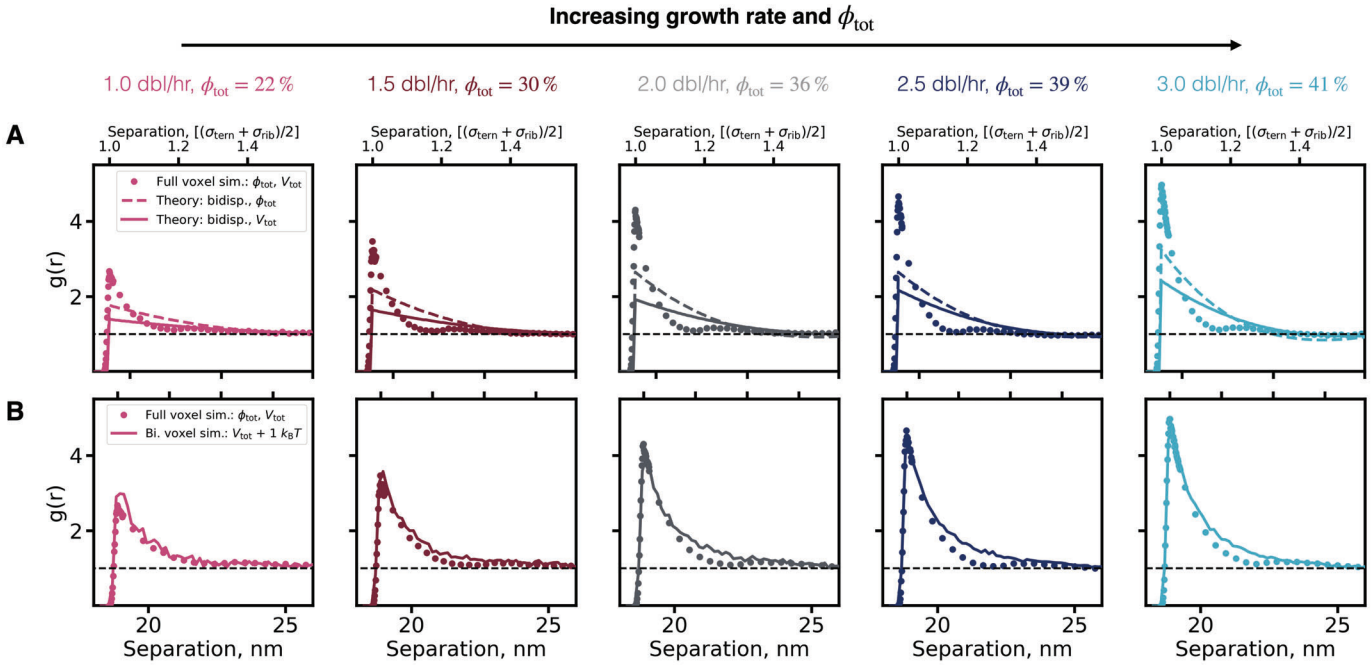

Figure S5: Small proteins in the *E. coli* cytoplasm induce depletion interactions of strength $\varepsilon_{\mathrm{t,r}} \approx 1\,k_{\mathrm{B}}T$ between translation molecules. (A). Radial distribution functions between ternary complexes and ribosomes, $g(r)$, calculated in simulations of translation voxels (symbols), highlight structural deviations from the ideal gas limit (dashed black line) across all growth rates. Analytical radial distribution functions, calculated for bidisperse suspensions of ternary complexes and ribosomes with the same abundances as in the full translation voxels, are also shown for systems with the same ϕ_{tot} (colored dashed line) and V_{tot} (colored solid line). Volume fraction alone is insufficient to recover the microstructure observed in full cytoplasmic voxels (i.e., the peak at contact, $18.9\,\mathrm{nm}$), suggesting the presence of depletion interactions. **(B)**. Bidisperse systems with added $\varepsilon_{\mathrm{t,r}} = 1\,k_{\mathrm{B}}T$ Yukawa attractions (solid lines) recover the contact peaks of the tridisperse $g(r)$, across all growth rates, thus estimating the strength of the depletion interaction.

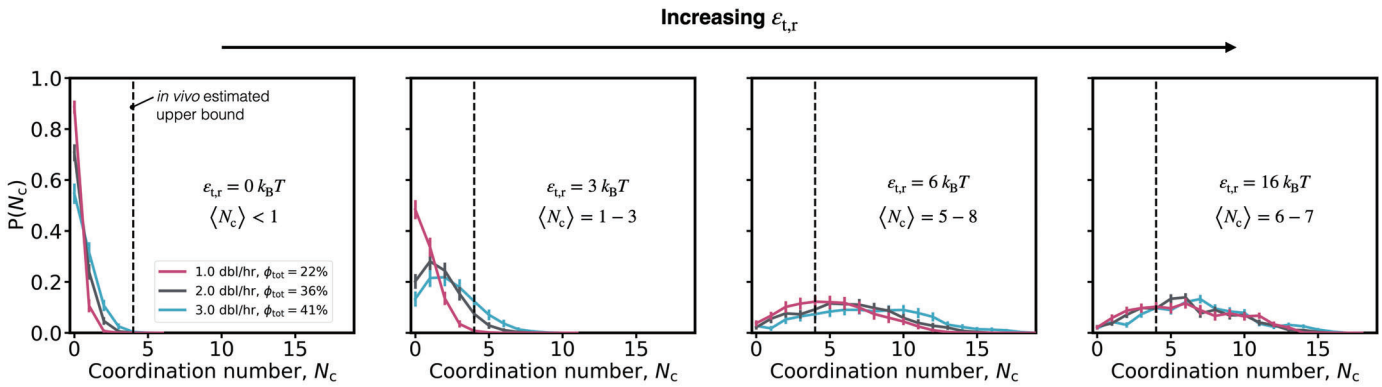

Figure S6: Strong isotropic $\varepsilon_{\mathrm{t,r}} \approx 6 - 16\,k_{\mathrm{B}}T$ attractions drive unphysiological coordination numbers of ternary complexes around ribosomes. Coordination number distributions highlight an increase in the number of ternary complexes bound to each ribosome, both with increasing growth rate (red to grey to blue) and attraction strength (left to right). The average number of ternary complex contacts per ribosome, $\langle N_{\mathrm{c}} \rangle$, exceeds the *in vivo* estimate of 4 ternary complexes per ribosome (vertical dashed black line, [17]) for attraction strengths $\varepsilon_{\mathrm{t,r}} > 6\,k_{\mathrm{B}}T$. In our model, isotropic attraction allows a maximum of $N_{\mathrm{c}} = 32$ based on close packing of spheres of size $a_{\mathrm{tern}} = 5.9\,\mathrm{nm}$ around spheres of size $a_{\mathrm{rib}} = 13\,\mathrm{nm}$ [56].

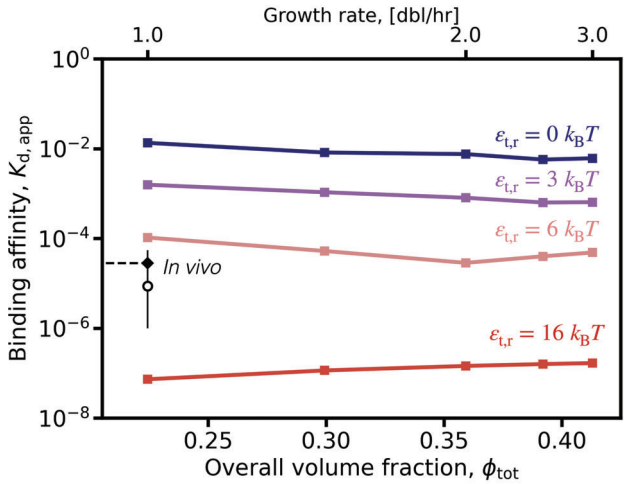

Figure S7: Validation of the calculation of $K_{\mathrm{d,app}}$ using *in vivo* measurements. Apparent binding affinity measurements, calculated via Eq. 11, are plotted for the interaction between ternary complexes and ribosomes in *E. coli* translation voxels with isotropic attraction strengths of $\varepsilon_{\mathrm{t,r}} = 0 - 16\,k_{\mathrm{B}}T$ (same data as in Fig. 3). The measured *in vivo* value at a growth rate of 1.0 dbl/hr is shown (♦), from [17]. Validation of Eq. 11 is marked (○), assuming four binding sites on the ribosome, 60% of ternary complexes bound, and abundances and densities of the translation voxel at a growth rate of 1.0 dbl/hr.

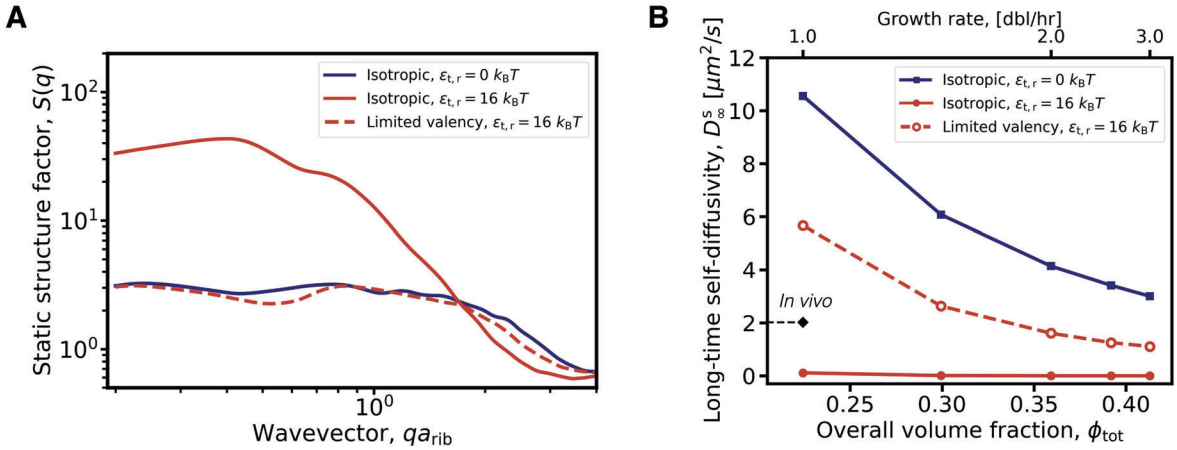

Figure S8: Limiting the valency of attractions between ternary complexes and ribosomes prevents arrested phase separation. (A). Static structure factor, $S(q)$, at a growth rate of 1 dbl/hr in the purely-repulsive limit (blue, solid line) and with isotropic (red, solid line) and limited valency (red, dashed line) attractions between ternary complexes and ribosomes. Limiting the interaction valency prevents the abundance of longer length-scale correlations observed in the isotropic case. **(B)**. Long-time self-diffusivity of ternary complexes as a function of growth rate and total volume fraction. The experimentally-observed apparent diffusivity is shown for a growth rate of 1.0 dbl/hr (♦) [17]. Limiting the interaction valency improves agreement with the in vivo measurement, without fully arresting dynamics as in the isotropic case. The remaining gap could be attributed to the limited temporal resolution of particle tracking experiments ($\sim 2\,\mathrm{ms}$), which are sufficiently large to sample the confinement in a given observation window. We thus might expect experimental measurements (♦) to be artificially low relative to our unbound simulations.

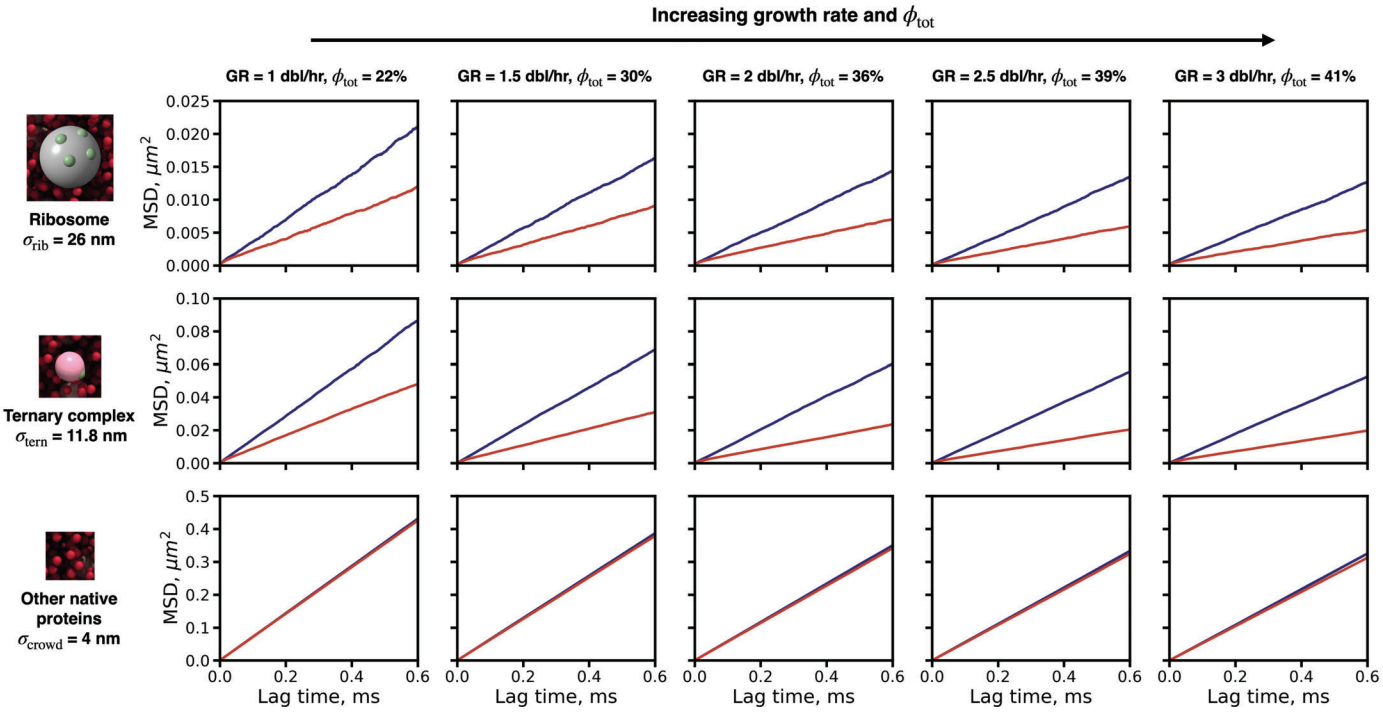

Figure S9: Limiting the valency of attractions between ternary complexes and ribosomes permits more particle mobility across growth rates. Mean squared displacements versus lag time are plotted for ribosomes (top row), ternary complexes (middle row), and other native cytoplasmic proteins (bottom row), for each growth rate (left to right) and limited valency attraction strengths of $\varepsilon_{\mathrm{t,r}} = 0\, k_{\mathrm{B}}T$ (blue) and $\varepsilon_{\mathrm{t,r}} = 16\, k_{\mathrm{B}}T$ (red).

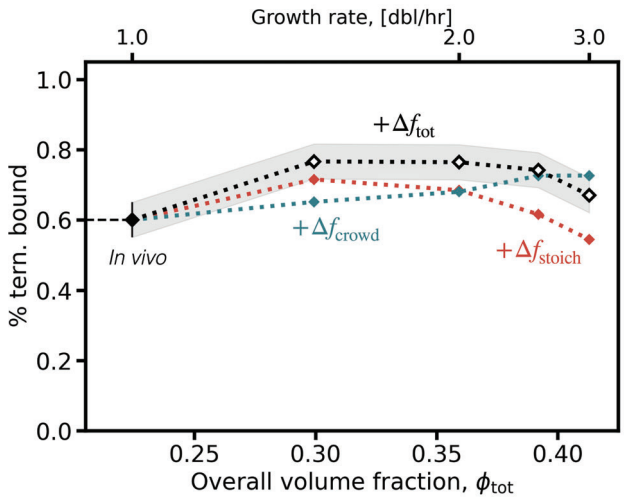

Figure S10: *In vivo* co-localization of ternary complexes and ribosomes is projected to increase non-monotonically as a function of growth rate. Extrapolation of the measured *in vivo* fraction of ribosome-bound ternary complexes, f, at 1 dbl/hour (black solid diamond) to higher growth rates (see Supplementary Methods). The change in co-localization due to entropic forces ($+\Delta f_{\mathrm{crowd}}$, teal) and changing relative stoichiometry ($+\Delta f_{\mathrm{stoich}}$, orange), assuming each L7/L12 is bound to one ternary complex. These two contributions are summed to obtain the extrapolated *in vivo* prediction to higher growth rates ($+\Delta f_{\mathrm{tot}}$, black), including errors carried forward from the experimental measurement at 1 dbl/hour.

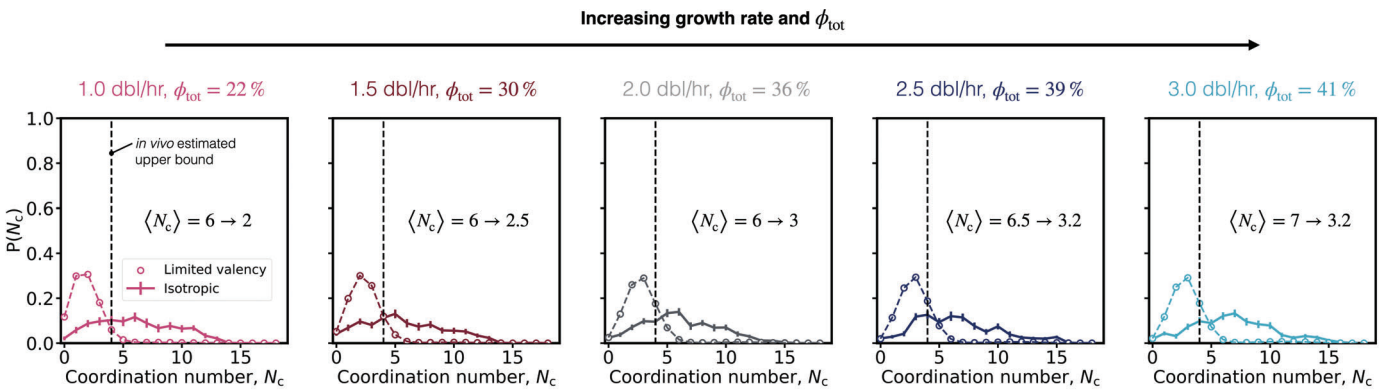

Figure S11: Limited valency attractions drive biofidelic co-localization of translation molecules, without higher-order microstructure. Coordination number distributions highlight an increase in the number of ternary complexes bound to each ribosome, both with increasing growth rate (red to grey to blue) and interaction valency (dashed versus solid lines) for attractions of strength $\varepsilon_{t,r} = 16\, k_B T$. The estimated maximum ribosome occupancy from experiments [17] is four ternary complexes per ribosome, marked by a vertical dashed line. A reduction in the average number of ternary complex contacts, $\langle N_c \rangle$, felt by ribosomes is noted for the isotropic case relative to the limited valency case, at each growth rate (left to right).

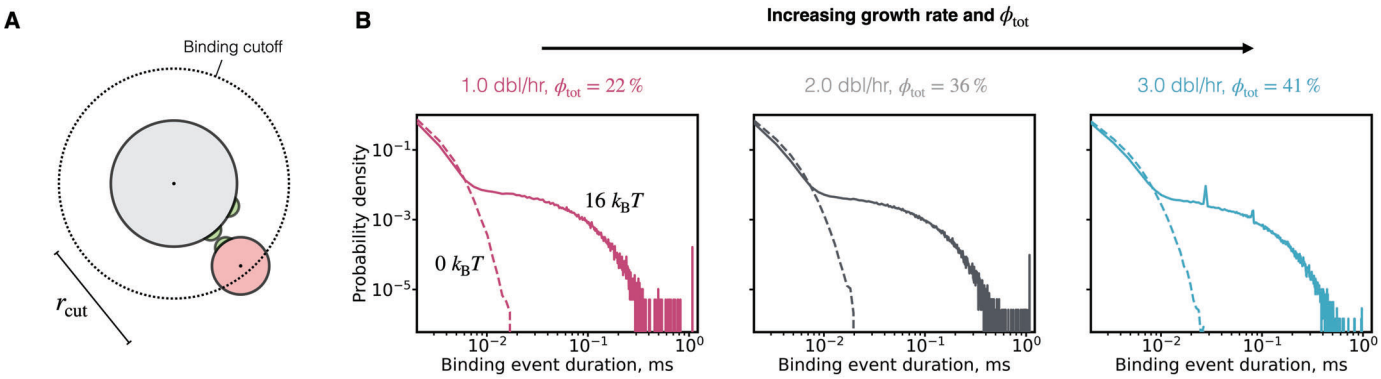

Figure S12: Probability distributions of the duration of physical ternary complex - ribosome binding events. (A). Schematic of binding cutoff between limited valence ternary complexes and ribosomes, chosen to be $r_{\mathrm{cut}} = 2.1\,\mathrm{nm}$ based on the radius of the binding site protrusions and width of the attractive potential well. **(B)**. Probability density function of the duration of binding events, defined as when a ternary complex and ribosome come within a bond distance (r_{cut}). Across all studied growth rates (left to right), purely entropic binding events are brief, lasting at most $\sim 20\,\mu\mathrm{s}$ (dashed lines, $0\,k_{\mathrm{B}}T$). The strong limited valence case (solid lines, $16\,k_{\mathrm{B}}T$) show binding times up to 1 ms, on the order of chemical reaction timescales, but below the upper limit of $2\,\mathrm{ms}$ inferred from experiment [17].

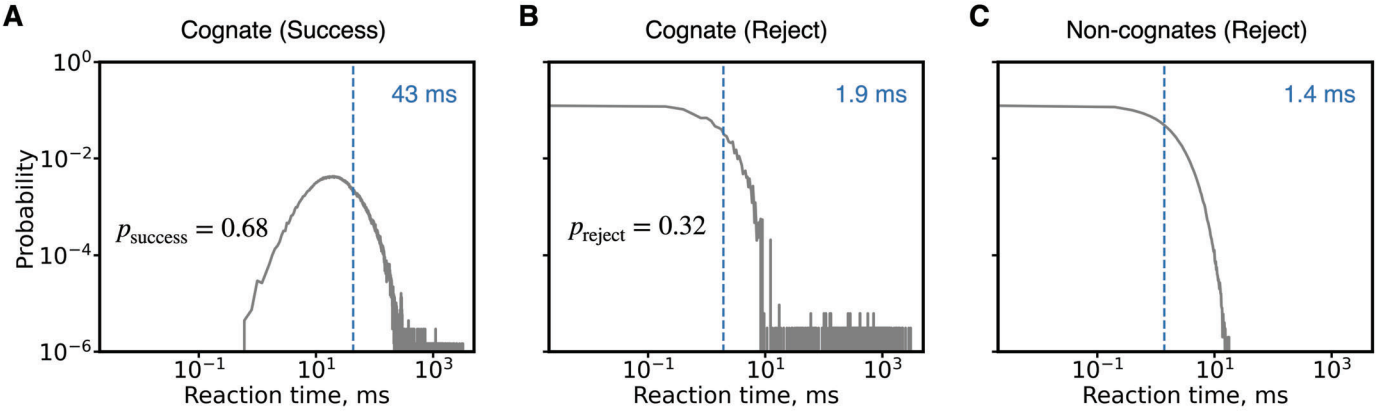

Figure S13: Distribution of time spent by cognate and non-cognate ternary complexes in reactions with ribosomes, computed by sampling kinetic trajectories. (A). Reaction times for cognate ternary complexes that successfully react (with probability p_{success} inset, black) and **(B)** those that are rejected (with probability p_{reject} inset, black). **(C)** Reaction times for non-cognate ternary complexes, of which all are rejected. In each plot, the average latency is marked (vertical blue dashed line, displayed at top right).

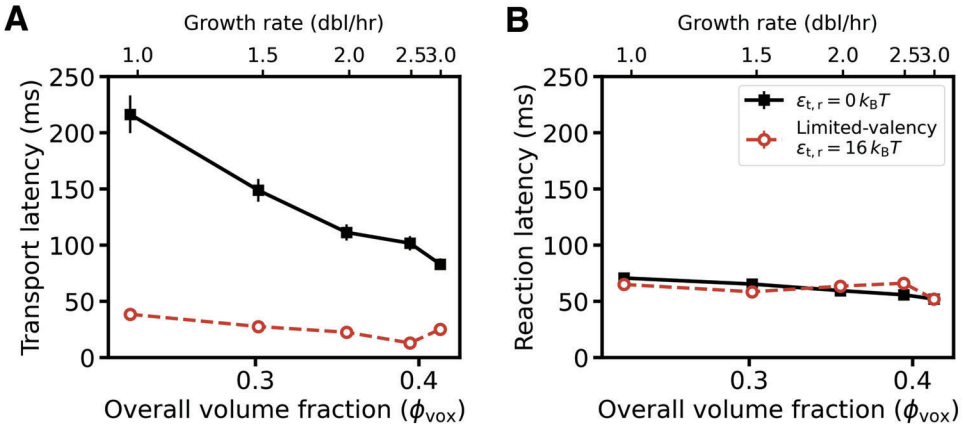

Figure S14: EF-Tu·L7/L12 interactions speed elongation by facilitating faster transport. Simulation results from translation voxels without attractions (black line, [3]) and with limited-valency attractions between ternary complexes and ribosomes (red line, this work). **(A)** Transport latency, which decreases with increasing growth rate (left to right), is reduced by pre-loading of ternary complexes onto ribosomes. **(B)** Reaction latency is unchanged by cognate-independent pre-loading.

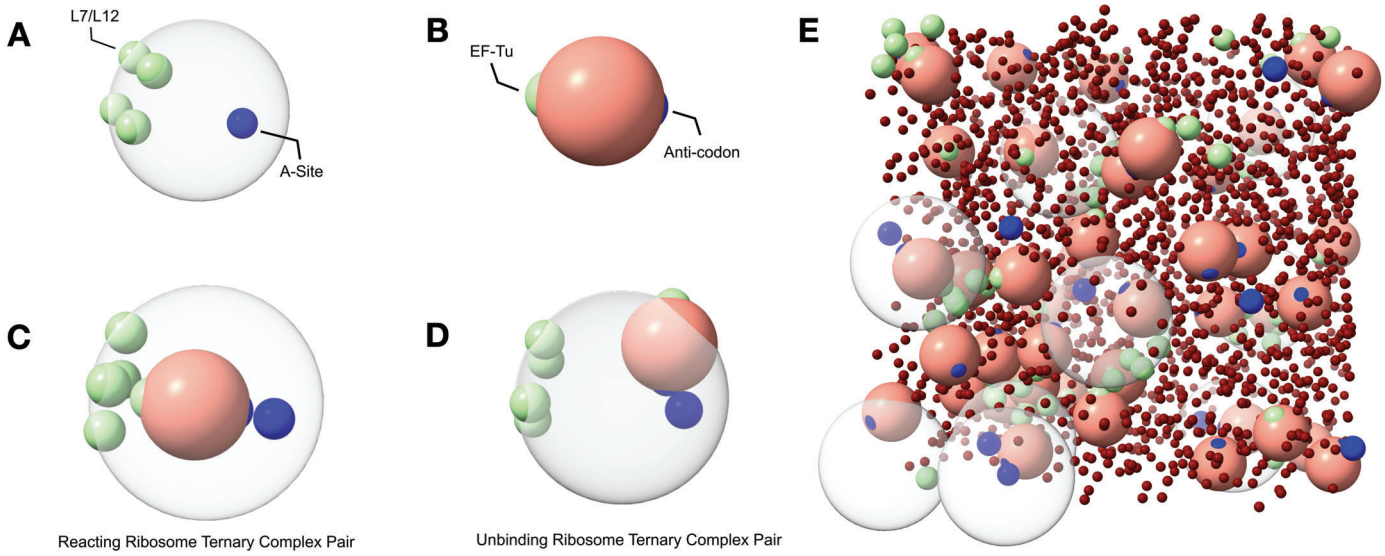

Figure S15: Schematics for modeling physical interactions and chemical reactions in translation voxels of the E. coli cytoplasm in LAMMPS. (A) Ribosomes (grey) are represented as rigid bodies with patches representing four L7/L12 subunits (green) and one internal A-site codon (blue). **(B)** Ternary complexes (pink) are represented with as rigid bodies with one EF-Tu (green) and anti-codon patch (blue). **(C)** After a reaction begins, the ternary complex is internalized within the ribosome by turning off the hard sphere repulsion and turning on a strong attraction between the A-site and anticodon. During reactions, other ternary complexes are allowed to occupy the three free L7/L12 subunits but are not allowed to enter the ribosome. **(D)** Following the conclusion of a reaction, the ternary complex is released by a soft Morse repulsion between formerly reacting pairs. **(E)** Thousands of unique translation voxels are simulated to capture the physiological distribution of translation molecules and to calculate reaction, transport, and elongation latencies. Visualizations were created using UCSF ChimeraX [40].